Development of logic memory devices based on topological insulators

Rodrigo Antunes Mota
Master in Engineering Physics
Department of Physics and Astronomy
Faculty of Sciences of the University of Porto and Faculty of Engineering of the University of Porto
2025

Development of logic memory devices based on topological insulators

Rodrigo Antunes Mota

Project Report carried out as part of the Master in Engineering Physics

Department of Physics and Astronomy

2025

Supervisor
Prof. Dr. André M. Pereira, Auxiliar Professor, Faculty of Sciences of University of Porto

Co-supervisor
Dra. Ana L. Pires, Auxiliar Researcher, Faculty of Sciences of University of Porto

U.PORTO
FACULDADE DE CIÊNCIAS
UNIVERSIDADE DO PORTO

IFIMUP
Instituto de Física de Materiais Avançados, Nanotecnologia e Fotónica
Universidade do Porto

“ Nature uses only the longest threads to weave her patterns, so each small piece of her fabric reveals the organization of the entire tapestry ”

- Richard Feynman

Acknowledgements

I would like to express my deepest gratitude to everyone who contributed to the completion of this work.

First and foremost, I sincerely thank my advisor, Prof. André Pereira, for his invaluable guidance, support, and encouragement throughout the development of this research. I am also grateful to my co-advisor, Prof. Ana Pires, for her insightful advice and more than constructive feedback.

I extend my thanks to Mafalda Moreira, for her constant assistance and dedication and for wasting a lot of her valuable time with my work. I also acknowledge Prof. Gleb Kakazei and Prof. Sergiy Bunyayev for their support and expertise in the ferromagnetic resonance (FMR) measurements, as well as Klaas Wijnsma for the debates we had about the results.

I am grateful to Carlos Roque, whose help with scanning electron microscopy (SEM) was essential for this work, and to Cândida Neto, who oversaw the SEM experiments and provided valuable guidance.

I would like to thank the Universidade do Porto and the Institute of Physics of Materials (IFIMUP) for providing the facilities and resources that made this research possible.

Finally, I am deeply thankful to my family and friends for their unconditional support, patience, and encouragement throughout this journey.

Abstract

The integration of ferromagnets with topological insulators has attracted growing attention due to the possibility of exploiting spin–orbit effects for next-generation spintronic devices, yet achieving stable and flexible heterostructures remains challenging.

This work presents a systematic study of thin films of FeCo and heterostructures of $FeCo/Bi_2Te_3$ deposited on glass and Kapton substrates by DC magnetron sputtering . Structural and morphological characterization was carried out using Scanning Electron Microscopy (SEM), Energy Dispersive Spectroscopy (EDS), X-Ray Diffraction (XRD), and X-Ray Reflectivity (XRR), while magnetic properties were probed by SQUID magnetometry and Ferromagnetic Resonance (FMR).

XRD analysis confirmed that the FeCo films grew polycrystalline with a dominant (110) orientation, while SQUID magnetometry revealed robust ferromagnetism with saturation magnetization values ranging from 501–1200 emu/cm³ and coercivities ranging from 52-166 Oe, accompanied by well-defined hysteresis loops,with the exception of the 10 nm samples, with minor dependence on the substrate type.

For FeCo on glass, a saturation magnetization of 1148 emu/cm³ and coercivity of 90 Oe were obtained, while on Kapton the values were 1174 emu/cm³ and 100 Oe, indicating strong ferromagnetic behavior and only minor influence of substrate change.Across individual thicknesses, the Ms values showed a general increasing trend with thickness, with intermediate deviations likely due to microstructural effects. Important to identify that the iron cobalt alloy has 50:50 atom ratio ($Fe_{50}Co_{50}$) with 99.99% purity. The Kapton substrate used was a Kapton HN polyimide film was approx. 25 µm thick, (DuPont).

In $FeCo/Bi_2Te_3$ heterostructures, the samples with 100 nm of Bi_2Te_3 on top of 100 nm of FeCo showed saturation magnetization values of 961 emu/cm³ (glass) and 893 emu/cm³ (Kapton), with coercivities of 91 Oe and 89 Oe, respectively, confirming that the substrate exerts little effect on the overall magnetic response.Other thicknesses showed Ms values ranging from 638 to 1.279 emu/cm³ depending on substrate and film thickness, while Hc varied from 82 to 183 Oe, highlighting the subtle interplay between thickness, substrate, and the presence of Bi_2Te_3.

However, surface roughness and crack formation strongly depended on substrate type and thickness. The addition of the Bi_2Te_3, layer preserved the ferromagnetic response of FeCo, revealed diffraction peaks consistent with the topological insulator, and produced

broader FMR lines, consistent with polycrystalline growth and structural defects.

These results demonstrate that $FeCo/Bi_2Te_3$ heterostructures retain the desired ferromagnetic properties and represent a promising platform for exploring the interplay between ferromagnets and topological insulators.

These findings confirm that $FeCo/Bi_2Te_3$ heterostructures maintain robust ferromagnetism and compatibility with flexible substrates,with saturation magnetization and coercivity showing only minor variation with substrate type and predictable trends with film thickness, opening opportunities for next-generation spintronic devices that combine mechanical flexibility with topological protection.

Key words: $FeCo;Bi_2Te_3$;topological insulator, spintronics, thin films, magnetron sputtering

Resumo

A integração de ferromagnetos com isolantes topológicos tem atraído crescente atenção devido à possibilidade de explorar efeitos spin–órbita em dispositivos espintrónicos de próxima geração, mas a obtenção de heteroestruturas estáveis e flexíveis continua a ser um desafio.

Este trabalho apresenta um estudo sistemático de filmes finos de FeCo e heteroestruturas de $\mathrm{FeCo/Bi_2Te_3}$ depositados em substratos de vidro e Kapton por sputtering magnético DC. A caracterização estrutural e morfológica foi realizada utilizando Microscopia Electrónica de Varredura (SEM), Espectroscopia de Energia Dispersiva (EDS), Difração de Raios X (XRD) e Reflectividade de Raios X (XRR), enquanto as propriedades magnéticas foram investigadas por magnetometria SQUID e Ressonância Ferromagnética (FMR).

A análise de XRD confirmou que os filmes de FeCo cresceram policristalinos com orientação dominante (110), enquanto a magnetometria SQUID revelou ferromagnetismo robusto com valores de magnetização de saturação entre 501–1203 emu/cm³ e coercividades variando entre 52–166 Oe, acompanhadas de ciclos de histerese bem definidos, com exceção das amostras de 10 nm, apresentando dependência mínima do tipo de substrato.

Para o FeCo sobre vidro, foi obtida uma magnetização de saturação de 1148 emu/cm³ e coercividade de 90 Oe, enquanto no Kapton os valores foram de 1174 emu/cm³ e 100 Oe, indicando comportamento ferromagnético forte e apenas uma influência mínima da mudança de substrato. Entre as diferentes espessuras, os valores de M_s mostraram uma tendência geral de aumento com a espessura, com desvios intermédios provavelmente devido a efeitos microestruturais. É importante destacar que a liga de ferro-cobalto possui uma proporção atómica 50:50 ($\mathrm{Fe_{50}Co_{50}}$) com 99.99% de pureza.O substrato de Kapton utilizado foi um filme de poliamida Kapton HN com aproximadamente 25 µm de espessura (DuPont).

Nas heteroestruturas $/\mathrm{Bi_2Te_3}$, as amostras com 100 nm de $\mathrm{Bi_2Te_3}$ em cima de 100 nm de FeCo mostraram valores de magnetização de saturação de 961 emu/cm³ (vidro) e 893 emu/cm³ (Kapton), com coercividades de 91 Oe e 89 Oe, respetivamente, confirmando que o substrato tem pouco efeito na resposta magnética global. Outras espessuras apresentaram valores de M_s variando de 638 a 1.279 emu/cm³ dependendo do substrato e

da espessura do filme, enquanto H_c variou de 82 a 183 Oe, evidenciando a interdependência subtil entre espessura, substrato e presença de Bi_2Te_3.

No entanto, a rugosidade da superfície e a formação de fissuras dependeram fortemente do tipo de substrato e da espessura. A adição da camada de Bi_2Te_3 preservou a resposta ferromagnética do $FeCo$, revelou picos de difração consistentes com o isolante topológico e produziu linhas de FMR mais largas, coerentes com crescimento policristalino e defeitos estruturais.

Estes resultados demonstram que as heteroestruturas $FeCo/Bi_2Te_3$ mantêm as propriedades ferromagnéticas desejadas e representam uma plataforma promissora para explorar a interação entre ferromagnetos e isolantes topológicos.

Estas descobertas confirmam que as heteroestruturas $FeCo/Bi_2Te_3$ mantêm ferromagnetismo robusto e compatibilidade com substratos flexíveis, com magnetização de saturação e coercividade apresentando apenas variações mínimas com o tipo de substrato e tendências previsíveis com a espessura do filme, abrindo oportunidades para dispositivos espintrónicos de próxima geração que combinam flexibilidade mecânica com proteção topológica.

Palavras Chave: $FeCo$;Bi_2Te_3;isolador topológico, spintrónica, filmes finos, magnetron sputtering

Table of Contents

List of Figures

List of Tables

List of Abbreviations

TI	Topological Insulator
SOC	Spin-Orbit Coupling
TRS	Time-Reversal Symmetry
QSHE	Quantum Spin Hall Effect
QHE	Quantum Hall Effect
TSS	Topologically Protected Surface States
WAL	Weak Antilocalization
TMR	Tunneling Magnetoresistance
FM	Ferromagnetic
NM	Non-Magnetic
DFT	Density Functional Theory
LDA	Local Density Approximation
GGA	Generalized Gradient Approximation
AHE	Anomalous Hall Effect
SHE	Spin Hall Effect
ISHE	Inverse Spin Hall Effect
LSV	Lateral Spin Valve
XRR	X-Ray Reflectivity
XRD	X-Ray Diffraction
SQUID	Superconducting Quantum Interference Device
FMR	Ferromagnetic Resonance
VNA	Vector Network Analyzer
CPW	Coplanar Waveguide

PPMS	Physical Property Measurement System
SEM	Scanning Electron Microscopy
EDS	Energy Dispersive Spectroscopy
MR	Magnetoresistance
AMR	Anisotropic Magnetoresistance
MTJ	Magnetic Tunnel Junction

1. Introduction

1.1. Topological Insulators

1.1.1. Contextualization

Topological insulators (TIs) are a recently discovered class of quantum materials that have attracted great interest in physics and engineering due to their unique properties. These materials are characterized by being insulating in their interior, or "bulk," but highly conductive on their surface, where electrons can move without scattering and with extremely low energy losses. This behaviour arises from the non-trivial topology of their electronic band structure, intrinsically linked to strong spin-orbit coupling (SOC).[1][2]

These properties make TIs a promising platform for emerging technologies, particularly in quantum computing and spintronics.[1]

In quantum computing, topological insulators play a crucial role due to the robustness of their surface states against external perturbations such as impurities and disorder. This robustness is associated with time-reversal symmetry (TRS) and topological protection.[2][3]

In spintronics, topological insulators offer unique opportunities for controlling and manipulating the spin of electrons in addition to their charge. Thanks to the spin–momentum locking effect, electrons in surface states have their spin rigidly aligned with their direction of motion, enabling the development of spin-based logic and non-volatile memory devices, leading to greater energy efficiency compared to traditional electronic devices.

A related phenomenon is the Quantum Spin Hall Effect (QSHE), where edge channels support spin-polarized transport without dissipation, see Figure 1.1 Unlike the conventional Quantum Hall Efect (QHE), which requires an external magnetic field, the QSHE arises intrinsically from SOC.[1] [2] This effect forms the basis for potential TI-based memory and logic devices.

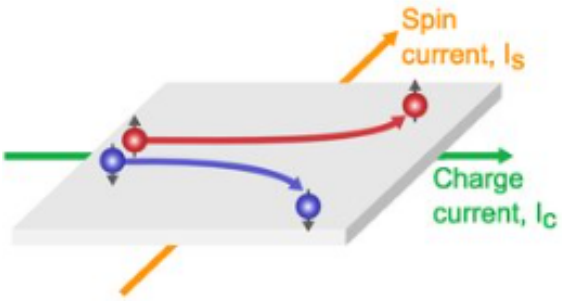

FIGURE 1.1: a)Quantum Spin Hall Effect illustration[4]

The energy gap is the difference between the valence band and the conduction band. In TIs, this gap exists in the bulk of the material, making it insulating in the inner region.

In TIs, due to spin–orbit coupling (SOC), the valence and conduction bands are "swapped" or inverted compared to conventional insulators. This inversion occurs due to relativistic interactions and is the origin of the non-trivial topology called inverted bands, see Figure 1.2.[1] [3]

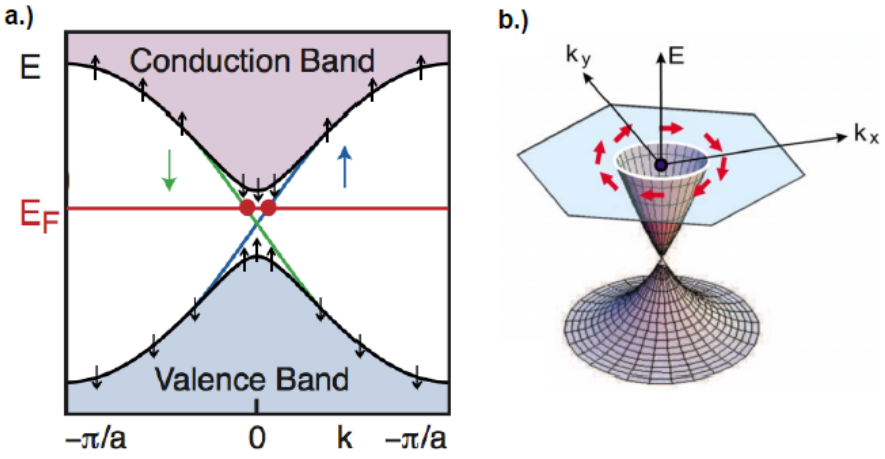

FIGURE 1.2: a)Band inversion results in topologically protected surface states in a bulk bandgap (green and blue lines)[1] b.) Spin-momentum locking on a topological surface state.[5]

When a TI is in contact with a normal insulator (such as a vacuum), conductive surface states appear that are protected by topological properties. These states are a consequence of bulk–boundary correspondence: the topology of the bulk requires that the edges be conductive to preserve the continuity of quantum properties.[3]

The Quantum Hall Effect (QHE) and TIs are related. In QHE, an external magnetic field creates conductive edge states. In TIs, intrinsic SOC plays a similar role but without

requiring an external magnetic field.

The surface states of TIs are robust against impurities and imperfections. This occurs due to the topological protection provided by TRS and spin–momentum locking. Scattering is prevented because the states remain coherent unless TRS is broken.[6]

TRS implies that the entire physical system remains invariant if time is reversed. In quantum mechanics, this means that wavefunctions evolve in such a way that there is no distinction between moving time forward or backward.

Scattering occurs when a wave or particle interacts with something that changes its direction or propagation state. This is undesirable because it leads to energy and information loss. However, TRS ensures that scattering satisfies symmetric properties.

For example, if a wave A is diffracted in direction B, TRS guarantees that a wave from B will be diffracted toward A. In systems with perfect TRS and no external perturbations (such as magnetic fields that break TRS), scattering does not occur because, in TRS, for every electron state with a given spin and momentum, there exists an opposite state. Thus, there are no two opposite paths for scattering to maintain the symmetry condition.

Similarly, backscattering is not allowed under these conditions.

Electrons in topological insulators have spin–momentum locking due to strong spin–orbit coupling. For backscattering to occur, the electron's momentum would have to change, which would imply a change in its spin.

This spin change is neither energetically nor dynamically favorable, and for it to happen, an external magnetic field breaking TRS would be required. [7]

Therefore, since momentum change does not occur without spin change, backscattering is suppressed under these conditions.

In the case of time-reversal symmetry breaking, the surface states are lost — surface states can acquire an energy gap and become insulating. This is the mechanism by which a TI can lose its surface conductivity.

1.1.2. Effects of Treatments

It has been observed, for example, that thin films of Bi_2Te_3topological insulators can be created through magnetic sputtering deposition, either on silica glass or on polyimide

substrates, followed by annealing at temperatures above 250 ℃. This process produces a polycrystalline structure with larger crystals and fewer defects, suggesting a reduction in the electrical contributions from the insulating bulk. [8]

In these thin films, between 20 K and 200 K, a metallic-like behavior is observed, indicating the presence of topological surface states (TSS). It has been found that higher annealing temperatures lead to improved results, enhancing crystallization and increasing crystal size.[8]

It has also been observed that quintuple layers exist — that is, a single structural unit composed of five atomic layers arranged sequentially, connected mainly by covalent bonds.[9] These quintuple layers are bound to each other via van der Waals bonds, which are crucial for supporting the formation of topologically protected surface electronic states. The existence of these layers also allows easier exfoliation, since van der Waals bonds are weak interactions that can be broken more easily.

It is also noted that Te–Te clusters can form, which are not typical in quintuple layers and are undesirable because they cause structural defects that affect the topological properties. These clusters can form under extreme pressure and temperature conditions, which promote structural rearrangements that bring tellurium atoms closer together, leading to the creation of such Te–Te clusters.[10]

Another observation is that the bulk conductivity of topological insulators depends on their thickness, highlighting the importance of controlling the geometry of the material.

From the analysis of the weak antilocalization (WAL) effect, measured through magnetoresistance at low temperatures when the material is subjected to external magnetic fields, it is confirmed that the films exhibit strong spin–orbit coupling, a key characteristic of topological insulators.[11]

In terms of physical stability, it is observed that topological insulators remain stable even under bending, with tests showing that even when bent to an angle of 83°, satisfactory performance is still obtained. [12]

1.2. Lateral Spin Valves

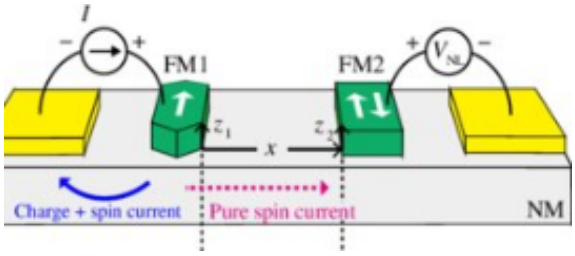

FIGURE 1.3: Lateral Spin Valve scheme [13]

Lateral spin valves (Figure 1.3) are used to control and manipulate the flow of electrons through their spin along the surface of a topological insulator. These devices allow the injection of spin-polarized electrons and can also be used to change the spin state.

In lateral spin valves, *tunneling magnetoresistance* (TMR) occurs. TMR is a magnetoresistive effect in spintronic devices in which the electrical resistance depends on the relative orientation of the magnetizations in ferromagnetic electrodes separated by a tunneling barrier.

A lateral spin valve typically consists of two ferromagnetic (FM) electrodes acting as the spin polarizer and spin analyzer, and a non-magnetic (NM) channel—usually a metal or semiconductor—serving as the transport medium for the injected spins. The injector and analyzer are designed with different coercivities, allowing the magnetic configuration to be switched between parallel and antiparallel states by applying an external magnetic field. [14]

The effective resistance of the spin valve is low when the analyzer spin orientation matches the magnetization of the polarizer, enabling efficient spin collection by the analyzer as seen in Figure 1.4.

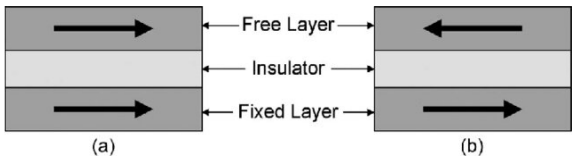

FIGURE 1.4: MTJ ferromagnetic layers in (a) parallel and (b) antiparallel configurations

The TMR value can be calculated as:

$$\mathrm{TMR} = \frac{R_{\mathrm{ap}} - R_{\mathrm{p}}}{R_{\mathrm{p}}} = \frac{(\beta - 1)^2}{4\beta} \tag{1.1}$$

where β is defined as the spin selectivity of the tunnel barrier, R_{ap} is the antiparallel resistance and R_p is the parallel resistance .

A high TMR value indicates a large difference between the antiparallel and parallel resistances, reflecting a significant difference in the density of states for spin-up and spin-down electrons. This separation between the parallel and antiparallel states corresponds, in memory device applications, to a clear distinction between the logical “0” and “1” levels, implying efficient devices, good spin polarization, and high-quality interfaces/barriers.

Conversely, a low TMR value indicates that the difference in resistance between parallel and antiparallel states is small, making it more difficult to distinguish magnetic states, thereby reducing device efficiency.

However, challenges remain in interfacing topological insulators with magnetic tunnel junctions [15] while maintaining both high TMR and the preservation of topological surface states (TSS).[9] [16] Photolithography can cause degradation, and annealing may lead to a reduction in electron diffusion.

1.2.1. Materials for Spin Valve Fabrication

In the fabrication of spin valves, the non-magnetic (NM) channel is typically made of copper, silver, or aluminum, while the ferromagnetic (FM) materials are commonly cobalt, permalloy (NiFe), and iron–cobalt (FeCo) alloys, such as FeCoB. In our case, however, the ferromagnetic layer is FeCo deposited on a glass substrate.

FeCo is preferentially used as the injector. In addition to having strong spin–orbit coupling, FeCo exhibits high spin polarization, meaning that a large fraction of the electrons transported by this alloy have their spins preferentially aligned in a single direction. This property is essential for spin injection into other materials, such as topological insulators, where the spin orientation of electrons must be precisely controlled. Being a ferromagnetic material with high magnetization, FeCo can generate strong magnetic fields that influence the motion of spin-polarized electrons. This is useful for aligning electron spins prior to injection into other materials.

Permalloy (NiFe) is often used as the analyzer because it has high magnetic permeability, meaning it responds easily to weak magnetic fields and exhibits high magnetization even under relatively small fields. This allows it to detect subtle changes in the magnetic field, making it ideal for sensing weak magnetic signals. It also has low magnetic anisotropy,

which means its magnetization can be easily oriented in any desired direction when an external magnetic field is applied.

It is worth noting that the thinner the NM material, the higher the tunneling magnetoresistance (TMR), the spin selectivity of the tunnel barrier, and the spin polarization.[17]

The propagation of spin—and the manner in which it propagates—depends on the properties of the non-magnetic material. The spin polarization in the NM can be described by:

$$P = \frac{D_{\uparrow}(E_F) - D_{\downarrow}(E_F)}{D_{\uparrow}(E_F) + D_{\downarrow}(E_F)} \tag{1.2}$$

where $D_{\uparrow}(E_F)$ is the density of states for spin-up electrons at the Fermi level E_F, and $D_{\downarrow}(E_F)$ is the density of states for spin-down electrons at E_F.[18]

Spin polarization measures the difference between the number of occupied states for spin-up and spin-down electrons at the Fermi level. This parameter is important in the study of lateral spin valves, as it allows the efficiency of spin injection to be quantified.

Another important parameter is the *spin diffusion length* λ_{SD}:

$$\lambda_{SD} = \sqrt{D\,\tau_{sf}} \tag{1.3}$$

where D is the diffusion constant of the material, and τ_{sf} is the spin relaxation time—the average time before spin orientation is lost. [19]

The spin diffusion length represents the average distance an electron can travel before losing its spin polarization. This model is used to characterize spin transport in non-magnetic materials where transport occurs via diffusion.

In the device under consideration (the lateral spin valve), λ_{SD} indicates the efficiency of spin propagation in the chosen material. To select the optimal NM material, one should choose a material with high electron mobility (and thus a higher D) and a long spin relaxation time, enabling electrons to travel further without spin interaction with the environment.

These quantities are related through the *non-local voltage* (V_{nl}):

$$V_{nl} = \frac{P^2 R_{sq} \lambda_{SD}}{2W}\, e^{-\frac{L}{\lambda_{SD}}} \tag{1.4}$$

where R_{sq} is the sheet resistance, W is the width of the NM layer, L is the separation

between the two FM electrodes (the analyzer and injector), and the exponential factor $e^{-L/\lambda_{SD}}$ describes the decay of spin polarization over distance L due to spin relaxation in the NM.

The non-local voltage is the voltage generated in the detector region of the device due to spin separation in the NM. It can be measured between the ferromagnetic analyzer and the NM using a nanovoltmeter. From this measurement, and using Eq. 1.4, one can determine both the spin polarization and the spin diffusion length, thus aiding in the fabrication of highly efficient lateral spin valves. [20]

1.3. Hall Sensors and Hall Effects

A Hall sensor operates according to the Hall effect, detecting a magnetic field and converting it into an electrical signal.

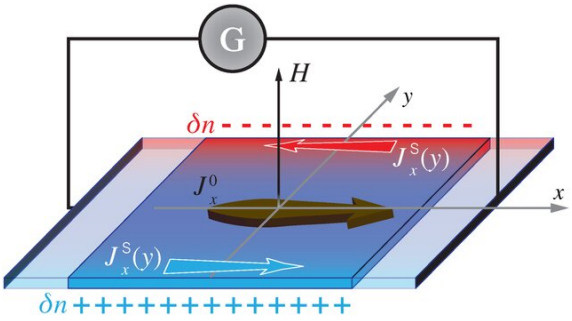

FIGURE 1.5: a)Schematic representation of the Hall effect under a static magnetic field H[21]

The Hall effect, discovered by Edwin Hall in 1878, is shown schematically in Figure 1.5, occurs when a current flows through a conductive or semiconductive material subjected to an external magnetic field. The charge carriers experience a force known as the Lorentz force, causing them to accumulate on one side of the material. This generates a potential difference perpendicular to both the direction of the electric current and the external magnetic field. The Hall voltage is given by:

$$V_H = \frac{IB}{nqt} \tag{1.5}$$

where I is the current through the material, B is the external magnetic field, n is the carrier density, q is the charge of the carriers, and t is the thickness of the material.

Hall sensors are typically made from semiconductors such as GaAs, due to their higher carrier mobility, which increases magnetic field sensitivity. The sensor has four electrical contacts: two to inject current and two transverse contacts to measure the potential difference produced by the Hall effect.

Several types of Hall effects can be detected with a Hall sensor:

Anomalous Hall Effect (AHE) Occurs in ferromagnetic materials where the electron spins align with the magnetic moment. When current flows, electrons with different spin orientations experience different forces due to spin–magnetic moment interactions, causing spins to accumulate on opposite sides of the material and generating a Hall voltage.[22]

Spin Hall Effect (SHE) Occurs in non-magnetic materials where an electric current induces a transverse spin current. Spin–orbit coupling causes electrons with opposite spins to move in opposite directions—spin-up electrons to one side, spin-down to the other.

Inverse Spin Hall Effect (ISHE) The reverse of the SHE: a polarized spin current generates a charge current perpendicular to the spin flow.

The spin current density generated by the SHE due to spin–orbit interaction in conductive materials can be expressed as:

$$\mathbf{J}_s = \sigma_{SH}\, \varepsilon_{ijk} E_j s_k \tag{1.6}$$

where $\mathbf{J}_s$ is the spin current density, σ_{SH} is the spin Hall conductivity (quantifying the efficiency of electric-to-spin current conversion), ε_{ijk} is the Levi–Civita tensor defining relative directions, E_j is the applied electric field, and s_k is the spin polarization component.

A simplified form is:

$$\mathbf{J}_s = \theta_{SH}\, \mathbf{J}_c\, \hat{s} \tag{1.7}$$

where $\mathbf{J}_c$ is the charge current density, θ_{SH} is the spin Hall angle (fraction of charge current converted into spin current, or vice versa for ISHE), and $\hat{s}$ is the unit vector of spin direction.[23]

From the ISHE, the transverse voltage measured across the width of the material (perpendicular to the spin current) is given by:

$$V_{ISHE} = \theta_{SH} \frac{J_s \rho t}{w} \tag{1.8}$$

where ρ is the material resistivity, t is the thickness, and w is the width of the material.

The spin current can then be calculated as:

$$I_s = \frac{2eV_{ISHE}\lambda_{SD}A}{\theta_{SH}\hbar\rho t} \tag{1.9}$$

where A is the cross-sectional area of the spin current path, e is the electron charge, λ_{SD} is the spin diffusion length, and $\hbar$ is the reduced Planck constant. [24]

These equations enable the quantification and evaluation of spin currents in devices, allowing extraction of key parameters such as the spin Hall angle and spin diffusion length.[25]

1.4. Analysis of Topological Insulators

The analysis of topological insulators can also be performed using *Density Functional Theory* (DFT), a computational method based on quantum mechanics used to investigate the electronic structure of materials.

In this context, for the study of topological insulators, the *Local Density Approximation* (LDA) and the *Generalized Gradient Approximation* (GGA) are typically employed.

In LDA, the exchange–correlation energy is assumed to be a function of the local electron density, making it suitable for systems with nearly uniform electron densities. The GGA extends LDA by including the gradient of the electron density, improving accuracy for systems with more complex electronic distributions, such as topological insulators, where it better captures the intricacies of their band structures. [26]

1.4.1. Spin–Orbit Coupling Hamiltonian

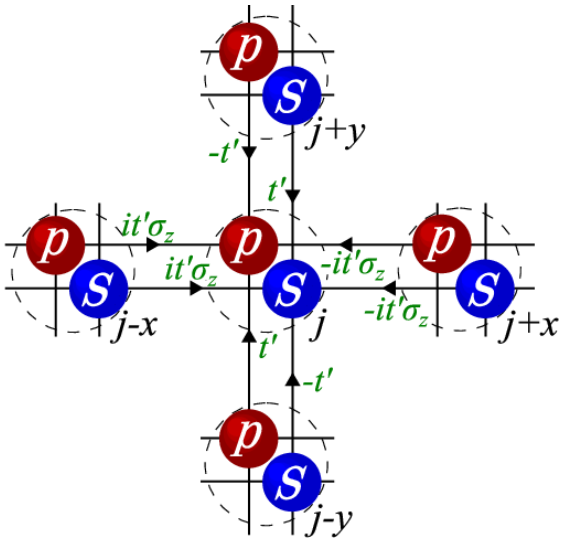

FIGURE 1.6: Schematic representation of the Hall effect under a static magnetic field H[27]

Spin–orbit coupling (SOC) arises from the interaction between the electron spins and their orbital motion in a potential V_0, see Figure 1.6 Its effect is described by the Hamiltonian:

$$H_{\mathrm{SOC}} = -\frac{\hbar}{4m^2c^2}\,\boldsymbol{\sigma}\cdot\nabla V_0 \tag{1.10}$$

where m is the electron mass, c is the speed of light, and σ is the vector of Pauli matrices representing the spin.

For potentials with spherical symmetry, this reduces to:

$$H_{\mathrm{SOC}} = \lambda\,(\mathbf{L}\cdot\boldsymbol{\sigma}) \tag{1.11}$$

where λ is the SOC strength and $\mathbf{L}$ is the orbital angular momentum operator.[25]

1.4.2. Classes of topological insulators

The most widely investigated TIs for device applications can be broadly classified into several material families.

The Bismuth Chalcogenites (Bi_2Te_3, Bi_2Se_3,Sb_2Te_3):This family represents the prototypical three-dimensional TIs. Among them, Bi_2Se_3 and Bi_2Te_3 are the most studied due to their relatively large bulk bandgaps, simple surface-state band structures, and availability of high-quality thin films. Bi_2Te_3, in particular, exhibits a single Dirac cone in its surface

electronic structure, as confirmed by ARPES studies [28]. These materials have been widely integrated with ferromagnetic metals and insulators to probe proximity-induced magnetism, spin torque generation, and spin pumping.[29]

The Heusler Compounds and Ternary TIs, such as Bi_2Te_2Se, are a class of materials that since have various ordered phases such as ferromagnetic and superconducting phases, it is possible to fabricate TI-based heterostructures that exhibit interesting topological magnetoelectric phenomena and Majorana fermions.[30]

The Topological Crystalline Insulators, such as $SnTe$ where the surface-state protection derives from crystalline symetries instead of the time-reversal symmetry.[31]

The Two Dimensional (2D) Quantum Spin Hall Insulators, such as $HgTe/CdTe$, where changing the thickness of $HgTe$ the quantum well past a critical value the system transitions from a normal insulator to an inverted band structure characteristic from the topological insulators [32]

1.5. Motivation

Despite the growing interest in ferromagnet/topological insulator heterostructures, several gaps remain in the literature. In particular, most studies have focused on materials such as Fe, Co, or Py (NiFe), while systematic investigations of $FeCo$ combined with Bi_2Te_3 are still limited. $FeCo$ is an attractive ferromagnet due to its high saturation magnetization, tunable anisotropy, and good thermal stability, making it highly relevant for spintronic applications. On the other hand, Bi_2Te_3 is a well-established topological insulator, with strong spin–orbit coupling and potential to host spin–momentum–locked surface states. The combination of these two materials is therefore promising for exploring spin–orbit phenomena and magneto-transport effects in hybrid systems.

However, little is known about how the choice of substrate (rigid vs. flexible) influences the structural integrity, magnetic response, and overall stability of $FeCo/Bi_2Te_3$ heterostructures, since very little literature is found on flexible substrates specially on kapton, being the majority of the literature on kapton substrate being of other materials such as $CoFeB$ [33] and $FeGa$ [34]. This is particularly relevant for the development of flexible spintronic devices, where mechanical adaptability must be achieved without compromising magnetic performance.

In this work, we focus on $FeCo/Bi_2Te_3$ heterostructures, aiming to explore their structural and magnetic properties and assess their potential for logic and memory devices, including their integration on flexible substrates such as Kapton.

2. Samples

2.1. Fabrication

2.1.1. Materials

Thin films were fabricated using the magnetron sputtering technique.The equipment used was a CY Scientific Instrument DC-Sputtering device.

$FeCo$ samples with thicknesses of 10 nm, 25 nm, 50 nm, 100 nm, and 200 nm were prepared. In addition, samples of FeCo with a top layer of Bi_2Te_3 were fabricated with the following thickness combinations: 25 nm of $FeCo$ + 100 nm of Bi_2Te_3, 50 nm of $FeCo$+ 100 nm of Bi_2Te_3, 100 nm of $FeCo$ + 100 nm of Bi_2Te_3, and 100 nm of $FeCo$ + 20 nm of Bi_2Te_3 and 100 nm of $FeCo$ + 50 nm of Bi_2Te_3 . These samples with both materials were referred a lot of times during the thesis as 25M100T, 50M100T, 100M100T, 100M20T,100M50T, respectively, for simplicity, where the M stands for Magnetic material and the T for Topological material.

For each thickness, two substrates were used in the deposition (one is glass silica substrate and the other is kapton substrate).

The iron cobalt targets are Fe50Co50 with a purity of 99.99% and the bismuth telerium targets are from with a purity of 99.999%.

2.1.2. Cleaning substrates process

The glass substrates were sequentially cleaned with acetone, ethanol, and deionized water to remove contaminants and ensure good film adhesion.

In contrast, Kapton substrates have a relatively inert surface, which can lead to poor adhesion of sputtered films such as FeCo.

Therefore, a pre-treatment was necessary to enhance adhesion. The Kapton substrates were cleaned by immersion in KOH solution for 1 hour, followed by rinsing with water, immersion in HCl for 5 minutes, and a final rinse with water. This procedure improves surface roughness and increases surface energy, which are essential for achieving strong film adhesion, as previously reported.[35] [36]

2.1.3. Deposition conditions

All depositions were carried out in the same chamber under previously optimized conditions by the team.

(a) **(b)**

FIGURE 2.1: a)Deposition chamber used b)Control tower of the deposition process

The conditions were for the Bi_2Te_3 an applied current of 20 mA, argon gas flow of 50 sccm (Standard Cubic Centimeters per Minute) and a sample table rotation of 60 rpm and for the FeCo an applied current of 50mA, argon gas flow of 50 sccm and a sample table rotation of 60 rpm.

Depositions commenced only after the pressure inside the deposition chamber reached order of magnitude of 10^{-4} Pa.

Samples on kapton and glass substrates with the same thickness were deposited simultaneously, ensuring thickness consistency between the two.

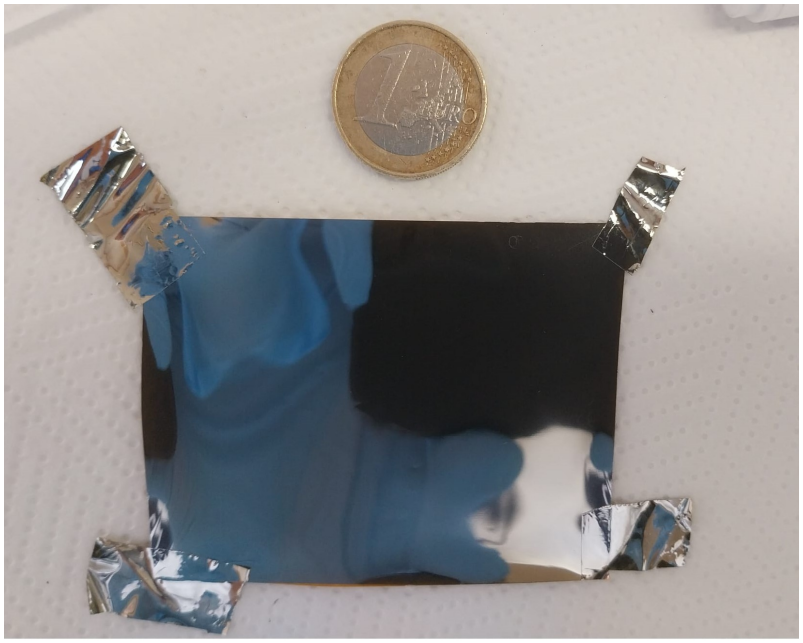

FIGURE 2.2: Sample post-deposition on kapton substrate

2.2. Characterization techniques

2.2.1. X-Ray Reflectivity (XRR)

XRR is a technique used for thin films using the reflection of the X-rays in the interfaces of the sample that can be used understand, the film thickness, the film density and the roughness of the interfaces.

This measurement was made in the Rigaku Smartlab Diffractrometer using Paralel-Beam geometry, varying the angle between 0° and 2.5°. The X-rays were obtained using the $CuK\alpha_1$ radiation being $\lambda \approx 1.542$.

2.2.2. X-Ray Diffraction (XRD)

XRD is a technique used to study the structural properties of crystalline materials. By analyzing the diffraction of X-rays from the atomic planes in the sample, it is possible to determine the crystal structure, lattice parameters, crystallite size, and the presence of different phases.

This measurement was carried out using the Rigaku Smartlab Diffractometer in Bragg-Brentano geometry, with the diffraction angle (2θ) varied from 10° to 80°. The X-rays were obtained using the $CuK\alpha_1$ radiation, with $\lambda \approx 1.542$ Å.

2.2.3. Superconducting Quantum Interference Device (SQUID)

SQUID magnetometry is a highly sensitive technique used to measure the magnetic properties of materials. It allows the determination of magnetization, magnetic susceptibility, and other magnetic responses as a function of temperature and applied magnetic field.

The measurements were performed using a Quantum Design MPMS SQUID magnetometer, in the temperature range of 300K, oscilating the field between -5000 Oe and 5000 Oe, with samples that were cut with approximately $0.7cm$ in length and $0.3cm$ in width, using a straw as a sample holder and cotton to stabelize the samples inside the straw. Since kapton is a flexible material the samples in kapton were also put inside a capsule to avoid the sliding of the sample during the measurement.

2.2.4. FMR (Ferromagnetic Resonance)

Ferromagnetic resonance (FMR) is a powerful technique to probe the dynamic magnetic properties of materials, as it allows the determination of parameters such as the effective magnetization, g-factor, and anisotropy fields by analyzing the resonance condition between microwave excitation and the precession of magnetization under an external magnetic field.

This measurements were conducted in the 1-20 GHz frequency range, employing a coplanar waveguide (CPW) connected to a Vector Network Analyzer (VNA Anritsu 37247D) and the external magnetic field is produced by Helmoltz coils.

2.2.5. Physical Property Measurement System (PPMS)

Electrical transport properties were studied using the Quantum-Design PPMS system, enabling the measurement of resistivity and Hall effect under controlled temperature and magnetic field conditions.

The sample is mounted on a PPMS puck using a standard 4-point contact configuration. A thin gold film is placed between the sample and the puck to improve thermal and electrical contact. Electrical connections are made with copper wires fixed to the sample using conductive silver paint. A piece of cigar paper is placed between the sample and the gold film to provide electrical insulation while maintaining good thermal conduction. This setup ensures reliable resistivity and magnetoresistance measurements while preventing short circuits.

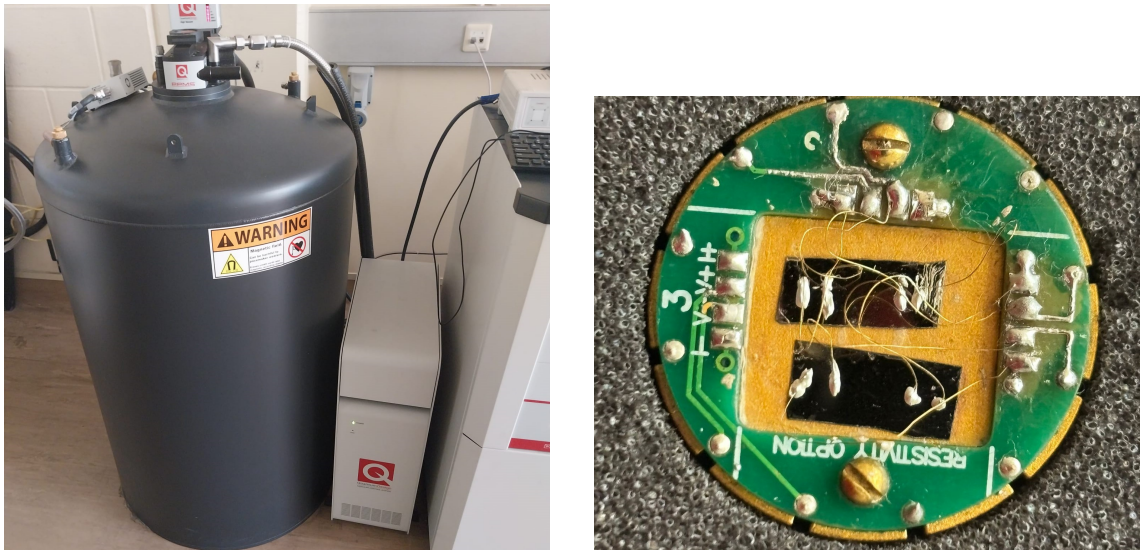

(a) **(b)**

FIGURE 2.3: a)PPMS device b)Sample preparation before measurement

The resistivity was measured using a standard four-probe configuration, in the temperature range of 2–300 K and magnetic fields up to 9 T.

2.2.6. Scanning Electron Microscopy (SEM) and Energy Dispersive Spectroscopy (EDS)

SEM was used to analyze the surface morphology and microstructure of the samples, providing high-resolution imaging of grain size, surface features, and defects. EDS was employed simultaneously to determine the elemental composition and homogeneity of the samples.

The measurements were performed using a FLEXSEM 1000 HITACHI.

2.2.7. Seebeck Coefficient

The Seebeck coefficient S is defined as:

$$S = -\frac{\Delta V}{\Delta T} \tag{2.1}$$

where:

- ΔV = thermoelectric voltage between the hot and cold ends of the sample
- ΔT = applied temperature difference

To determine S it is heated one end of the sample measuring with a voltimeter how the voltage across the sample varies with this temperature difference.

3. Magnetic FeCo thin films

3.1. Glass substrates

3.1.1. X-ray reflectivity (XRR)

The thickness of the produced FeCo films was determined using X-ray reflectivity (XRR).

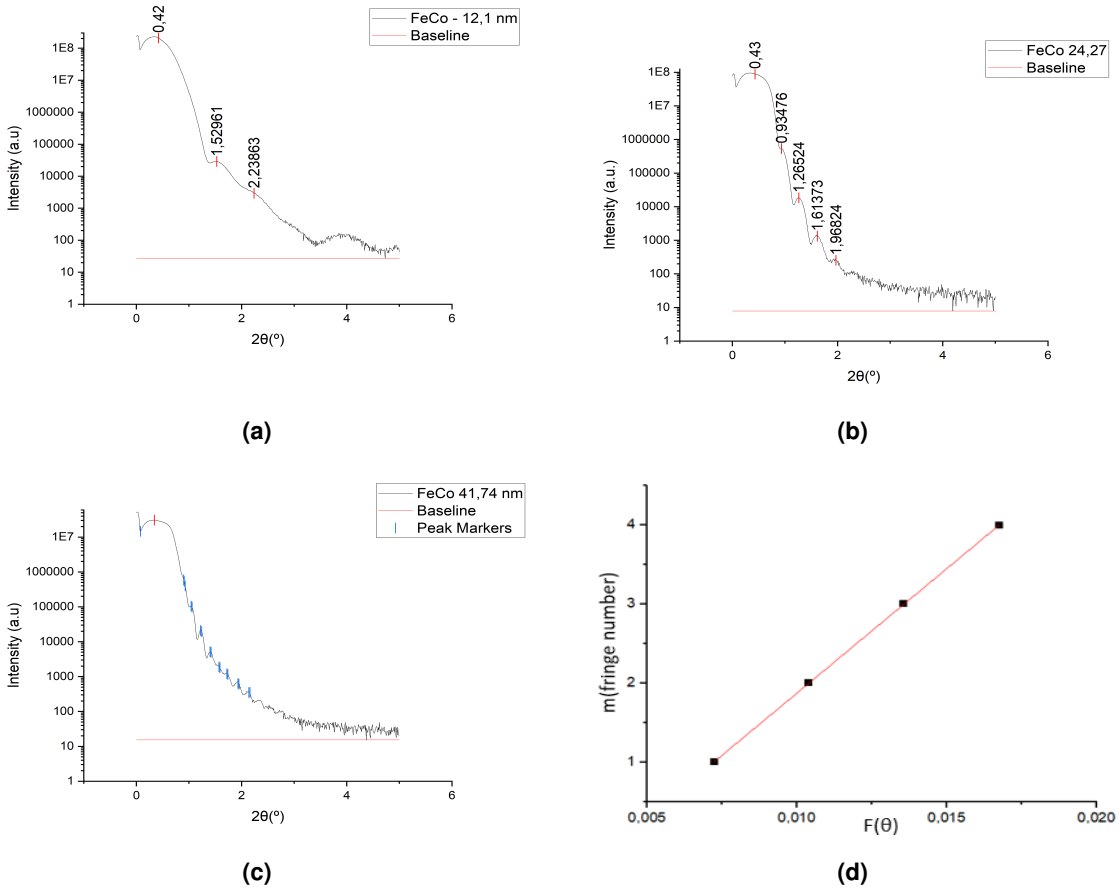

FIGURE 3.1: a)Example of a XRR pattern of FeCo sample with 12.1 nm of thickness. b)Example of a XRR pattern of FeCo sample with 24.27 nm of thickness. c)Example of a XRR pattern of FeCo sample with 41.74 nm of thickness. d)Linear Fit of to determine film thickness of the 24.27 nm sample

The characteristic Kiessig Fringes were observed(see on explie in Figure 3.1c this fringes only appear in homogeneous films with small surface roughness, confirming the quality

of the deposited layers .[37]

The film thickness was calculated using equation 3.1

$$m = -\frac{1}{2} + \frac{2t}{\lambda} F(\theta_m) \tag{3.1}$$

where m is the order of the fringes, θ_m is the angle of the maximum of the m correspondent fringe, t is total thickness of the sample, and $F(\theta_m)$ is a $F(\theta_m) = \sqrt{cos^2(\theta_C) - cos^2(\theta_m)}$ where θ_C is the critical angle, correspondent to the first fringe. The formula 3.1 is used to calculate the thickness as shown in Figure 3.1d.[38]

There were also made other XRR measurements in other parts of the sample being the final thickness calculated a weighted average between all the thicknesses calculated for the different measurements.

Sample Average (nm)	Measured values (nm)
1	12.1
2	24.27 ± 0.06
3	41.74 ± 0.08

TABLE 3.1: Measured thickness of the three possible samples

It was not possible to analyze every sample, only 3, since the limit of the XRR measurement its at the 100 nm of thickness.

This limit occurs since the mean path of the photon is insufficient to measure films beyond that thickness. Considering that XRR relies on the penetration and reflection of X-ray photons in the interface of the sample, a bigger thickness leads to bigger chance of absorption, scattering or diffuse reflection of the photons contributing to worse results. This leads to worse results to bigger samples with more than 100nm of thickness.[39]

Since it is not possible to use the XRR technique on the kapton substrate sample, and the kapton substrate sample was deposited simultaneously and so in the exact same conditions as the sample in glass substrate, it was assumed that the kapton substrate sample was the same thickness as calculated for the glass one.

3.1.2. Scanning Electron Microscopy (SEM)/Energy Dispersive X-ray Spectroscopy (EDS)

The surface morphology of the FeCo thin films was analyze by Scanning Electron Microscopy (SEM) as shown in Figure 3.2 for 25 nm and 200 nm deposited in glass substrate.

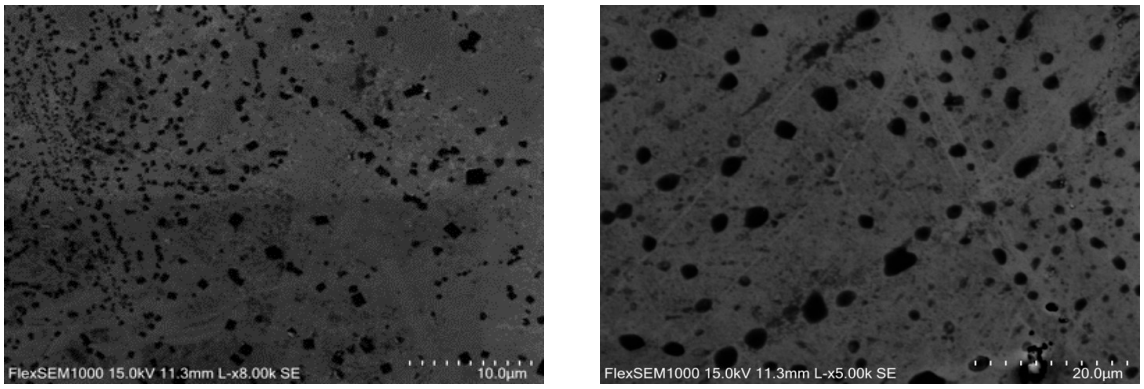

(a) **(b)**

FIGURE 3.2: a)SEM Image of the surface of the sample with 25 nm of FeCo on glass substrate b)SEM Image of the surface of the sample with 200 nm of FeCo on glass substrate

As depicted in the picture, no cracks were seen on the surface, indicating good mechanical integrity of the films. However, localized dark spots were detected on some regions of the sample, other than that no other big defects that could justify not ideal results were seen.

Those dark spots correspond likely to places where FeCo was not deposited.

Sample Size (nm)	Co (Norm.%)	Fe (Norm.%)
24.27	53.0	47.0
41.74	52.9	47.1
100.00	54.5	45.5
200.00	55.9	44.1

TABLE 3.2: Normalized atomic percentages of Co and Fe for updated particle sizes.

Looking at Table 3.2, it is possible to see a similar quantity of both Fe and Co as expected (the biggest difference being in the 200nm sample of 55.9% of Co and 44.1% of Fe similar to the expected 50:50 ratio), this diference can be associated to the lack of precision of the measurement.

The films show the expected spectroscopy.

The 12.1 nm sample doesn't feature the table because of its small quantity of material made it impossible to detect the sample in the substrate with the available instruments.

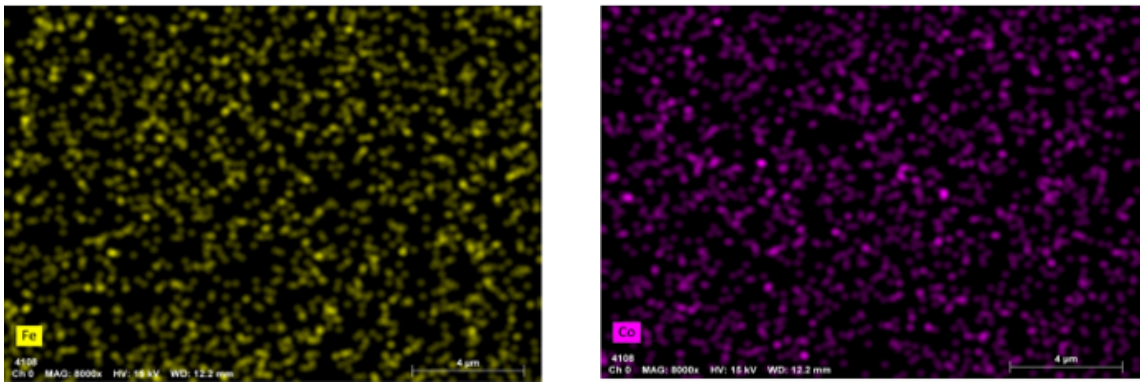

(a) **(b)**

FIGURE 3.3: a)Fe distribution in the 50 nm sample b)Co distribution in the 50 nm sample

It was also not seen any irregular distribution in the distribution or Fe or Co in Figure 3.3.

3.1.3. X-ray Diffraction (XRD)

X-Ray diffraction (XRD) was employed to investigate the crystallization of sputtered FeCo thin films .

The diffraction patterns are shown in Figure 3.4 for all the films deposited in glass (with thickness 12.1 nm, 24.27 nm, 41.74 nm, 100nm and 200 nm).

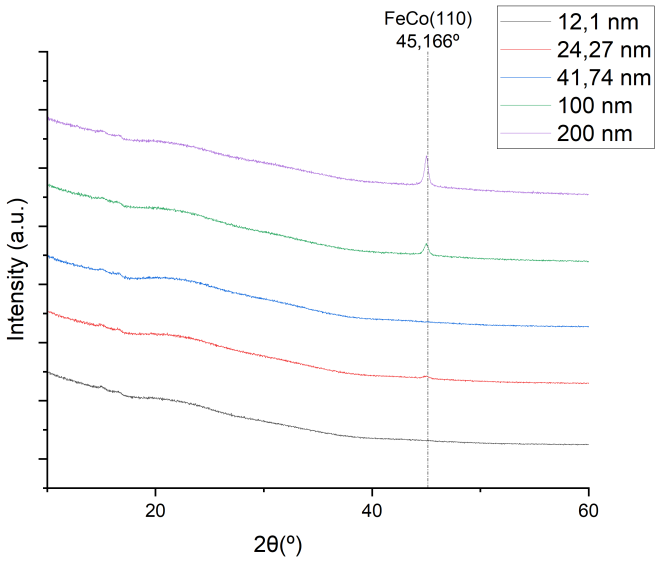

FIGURE 3.4: XRD spectrum of FeCo samples on glass substrate

A characteristic peak at 45.166° corresponding to the FeCo(110) reflection was observed in all of the samples with exception of those with nominal thickness 12.1 nm and 50 nm as we can see in Figure 3.4.

While the absence of the peak for the sample with 12.1nm of FeCo is expected, as the small amount of material could not be enough to present a visible peak for the 50 nm sample it would be expected the appearance of a peak.

This suggests the that the amount of crystalline material should be small.

3.1.4. Magnetic properties

The magnetic characteristics of the samples were studied by employing the Superconductive Quantum Interference Device (SQUID) magnetometry technique.

It was measured at 300K of FeCo samples sputtered in glass substrate with thicknesses of 12.1 nm, 24.27 nm, 50 nm 100 nm and 200 nm.

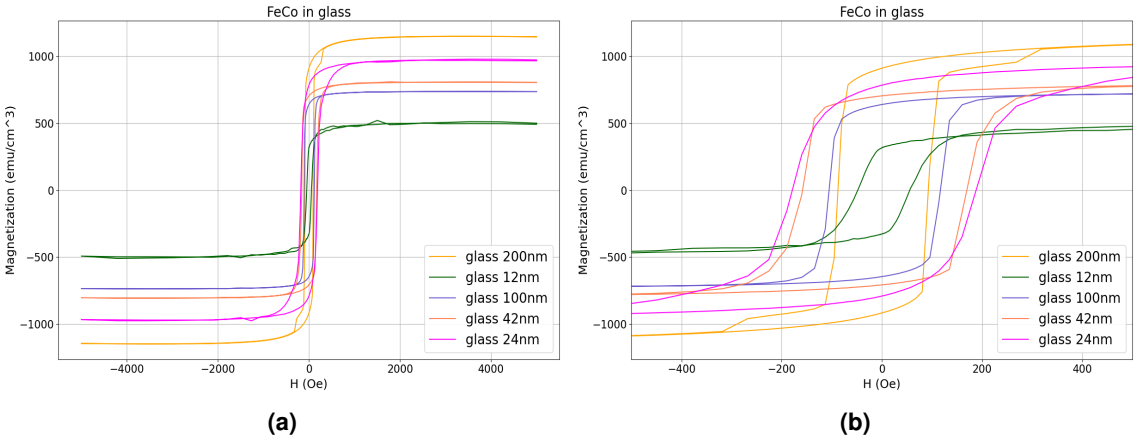

FIGURE 3.5: Isothermal M-H curve of FeCo in glass substrate of different thicknesses, right image is a zoomed in image of the left.

We could clearly see the hysteresis cycle showing the expected ferromagnetic behaviour and the appearence of magnetic domains in the material.

As we can see in Figure 3.5, the increasement of the magnetic field, leads to a bigger magnetization until it reaches the maximum value known as magnetization saturation, when the field is reduced the magnetization also reduces, not coming back to zero due to the remanant magnetization leading to the loop that can be seen in 3.5a. This behaviour is mirrored for positive and negative field applied.

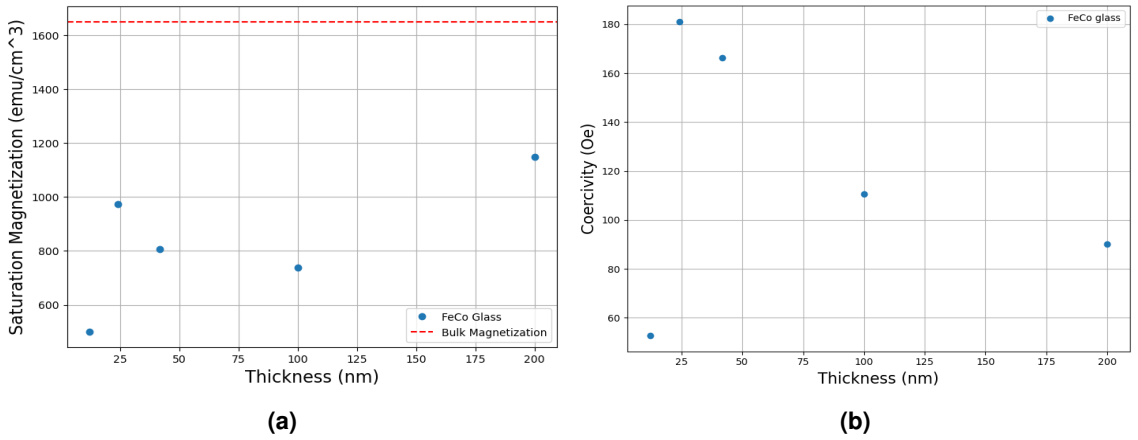

FIGURE 3.6: a)Graph of the saturation magnetization of all the samples measured in the SQUID b)Graph of the coercivity of all the samples measured in the SQUID

We can see in 3.6a a smaller magnetization saturation in the samples with thickness 12.1 nm and 100 nm.

From Figure 3.6a, it is evident that the saturation magnetization remains significantly below the bulk counterpart [40], reaching at most 71%. This clearly indicates that the

growth of this type of thin film involves the presence of several so-called ‘dead magnetic layers,’ which are typically formed at the interface and/or at the surface. Such behavior is expected, since thin film deposition inherently introduces interface effects that strongly influence the magnetic response.

The phenomenon becomes particularly pronounced in the thinnest sample (12 nm), where the saturation magnetization does not even reach 30% of the expected bulk value. This observation strongly suggests that the dominant contribution to the magnetic signal originates from the glass/FeCo interface, while the surface contribution appears to play a much less relevant role.

Overall, these results highlight the critical impact of interfacial phenomena on the magnetic properties of ultrathin films, emphasizing that even when nominal thickness increases, interfacial dead layers can substantially reduce the effective magnetization compared to the bulk counterpart.

For the sample 12.1 nm thick this result is to be expected, since the smaller amount of material may not be enough atomic layers so proper crystalization occurs.

For the 50 nm sample this results would not be the expected, however this results come in conformity with the XRD spectra analyzed already in 3.4, where there was already detected poor crystallization in this sample.

Looking at 3.6b we can see that the coercivity is low for the 12.1 nm sample, it reaches a maximum for the 24.27 nm sample, and then it reduces for bigger thicknesses.

This results come in conformity with the results obtained in the literature,where it was seen for example for thin films of FeCo had coercivity of 309 Oe, 220 Oe and 210 Oe for 50 nm, 100 nm and 200 nm thickness films, and magnetization saturation 1750 emu/cm^3, 1567 emu/cm^3 and 1560 emu/cm^3, respectively, in [41] or magnetization saturation of 1057 emu/cm^3 and coercivity of 100 Oe in a FeCo sample with 80 nm thickness in [42].

The reduction of the coercivity with the incresing thickness is caused by the reduction of the magnetic domains that are limited by the dimensions. For the lowest dimensions, the 12.1 nm sample, the coercivity increases since the sample behaves as a single-domain.

3.1.5. Ferromagnetic Resonance(FMR)

In order to characterize the dynamic magnetic properties of the samples, ferromagnetic resonance (FMR) measurements were performed, as this technique provides direct information on parameters such as effective magnetization, damping and magnetic anisotropy.

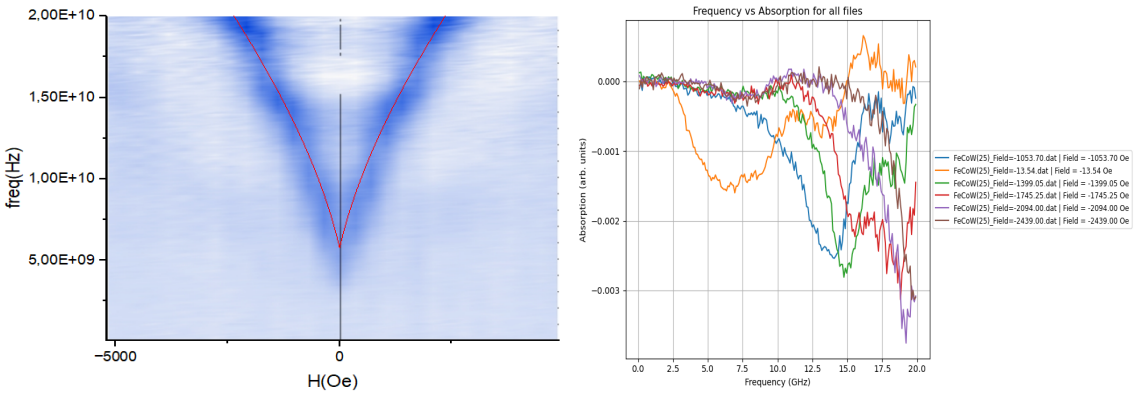

FIGURE 3.7: a)Conterplot of resonance frequency for each magnetic field for 25nm of FeCo on glass substrate b)FMR spectra for 50nm sample in glass substrate for different fields

To do the fit on Figure 3.7a it was used the Kittel fit:

$$f = \frac{\gamma}{2\pi}\sqrt{(|H_{res}| + H_{ani}) + (|H_{res}| + H_{ani} + 4\pi M)} \tag{3.2}$$

Using this equation it was possible to determine the magnetization and the anisotropy field trough the FMR, being detected very low anisotropy filed for every sample as we can see in Table 3.3.

Sample Thickness (nm)	Ha (Oe)	Ms(emu/cm^3)
10	No information	No information
25	-105 ± 40	1352 ± 100
50	-92 ± 47	1368 ± 217
100	-39 ± 47	1285 ± 82
200	No information	No information

TABLE 3.3: Magnetic anisotropy field (H_a) and Magnetization saturation (Ms) for different sample thicknesses.

The FMR analysis revealed a rather complex behaviour, primarily due to the resonance peak not being sharp or well defined, complicating the extraction the extraction of more precise information.

Despite this limitation, measurements were made across the set of samples. In the case of the 12.1 nm sample no fitting prcedure could be performed. This limitation is most likely associated with the extremely low magnetic moment of this ultrathin film, which, in combination with its behavior resembling a quasi–single-domain system (as already suggested by the coercive field observed in the M(H) loop), prevents the establishment of a clear resonance profile.

For the ramaining films, with the exception of the 200 nm sample which resonance could not be detected at all the extracted values of saturation magnetization are consistently slightly higher than those obtained from the static M(H) measurements.This apparent discrepancy can be rationalized by considering the intrinsic differences between the two techniques. While M(H) curves provide the effective magnetization of the entire film, including the contribution of magnetically “dead layers” at the interface and surface, the FMR experiment selectively probes the magnetodynamical response of the ferromagnetic regions.Consequently, FMR effectively yields the intrinsic saturation magnetization of the active ferromagnetic volume, thereby excluding the suppressed contribution from dead layers.[43]

A particularly noteworthy trend is observed in the anisotropy field, which systematically increases as the film thickness decreases. This thickness dependence reflects the growing importance of surface and interfacial contributions in ultrathin films, where reduced dimensionality enhances magnetic anisotropy. Such behavior strongly supports the interpretation that, as the thickness approaches the nanoscale limit, the system progressively evolves toward a single-domain regime. This evolution not only highlights the critical role of interfacial and finite-size effects in defining the static and dynamic magnetic response, but also underlines the necessity of employing complementary techniques (such as FMR and M(H)) to disentangle intrinsic from extrinsic contributions to the overall magnetic behavior.[44]

The saturation magnetization obtained here is bigger than the obatined in the SQUID. This would be expected since the magnetization in the SQUID is the magnetization at 300K, while in the FMR the magnetization measured is th e effective magnetization, since thermal excitations are ignored in the resonance formula being equal to what would be the magnetization saturation of the sample in SQUID at 0K.

However, it was not possible to identify any trend from the results because of the big error of the values.

The dificulty in differentiating peaks and the big broadening of the peaks as we can see in3.7b made it impossible to calculate the damping, since the damping would be very small this error was very significant and causes the impossibility of the calculations.

3.2. Flexible substrate: Kapton

3.2.1. Scanning Electron Microscopy (SEM)/Energy-Dispersive X-ray Spectroscopy (EDS)

The SEM (Scanning Electron Microscopy) was used to analyze the surface of the samples.

We used this technique to see if the samples had no defects that could be responsible for lower than ideal characteristics in the sample.

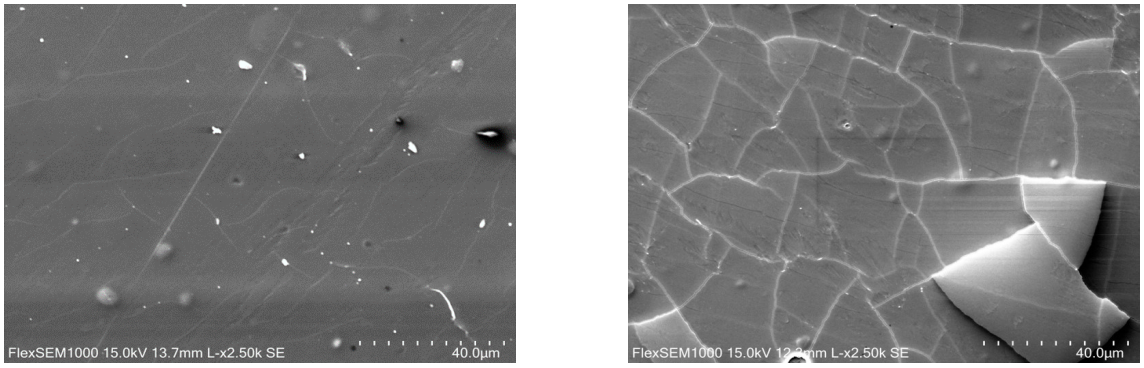

(a) **(b)**

FIGURE 3.8: a)Image of Scanning Electron Microscopy of 24.27 nm sample b)Image of Scanning Electron Microscopy of 200 nm sample

We can see in the images in 3.8 what would be the state of the surface of the samples in a grayscale image, where the bright zones simbolize the edges or rough surfaces of the sample.

It is verified the existence of some cracks on the sample, which appear more the thicker the sample is.

The thermal expansion mismatch between Fe–Co thin films and their supporting substrates is a critical factor in determining the structural and functional stability of the system. Fe–Co alloys present a thermal expansion coefficient in the range of 10–13 × $10^{-6}K^{-11}$, whereas Kapton exhibits considerably higher values, typically between 20 and

30 × $10^{-6}K^{-1}$. In contrast, glass substrates show much lower coefficients, around 8–9 × $10^{-6}K^{-1}$ for soda-lime glass and approximately 3.3 × $10^{-6}K^{-1}$ for borosilicate glass.[45]

When FeCo films are deposited on Kapton, the large thermal expansion mismatch generates significant interfacial stresses, particularly during thermal cycling or post-deposition cooling. These stresses are only partially accommodated by the flexibility of the polymer substrate, and in many cases lead to the nucleation and propagation of cracks across the film. The presence of cracks is a direct manifestation of the inability of the FeCo layer to elastically accommodate the strain imposed by the underlying Kapton, resulting in a loss of structural continuity. This degradation compromises not only the mechanical integrity but also the magnetic uniformity of the films, since cracks act as pinning centers for domain walls and induce local variations in coercivity.

On the other hand, FeCo films grown on glass do not exhibit such pronounced cracking phenomena, due to the smaller difference in thermal expansion coefficients. In this case, the main drawback arises from the rigidity of the glass substrate, which does not permit strain relaxation through bending, but still ensures mechanically continuous and magnetically more homogeneous films.

Depositing a buffer layer prior to FeCo could be a solution to give thermal stability of the substrate, making it more resistant to heating during subsequent deposition.

Sample Size (nm)	Co (Norm.%)	Fe (Norm.%)
12.1	53.9	46.1
24.27	57.1	42.9
41.74	50.6	49.4
200.00	56.8	43.2

TABLE 3.4: Normalized atomic percentages of Co and Fe for different particle sizes.

On the EDS it was possible to identify and quantify the Fe and Co present in the sample.

It is seen again ratios very similar to 50:50 between Fe and Co in all of the samples, being that the differences can be explained by the small precision of the EDS for such a thin sample.

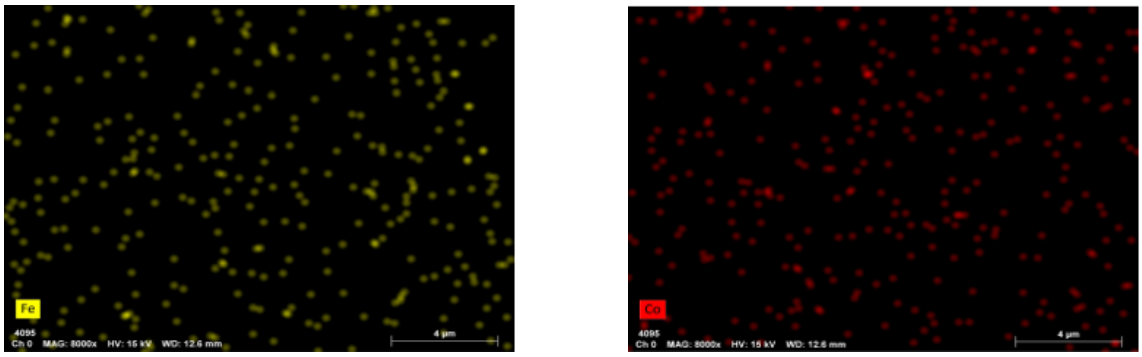

FIGURE 3.9: a)Fe distribution in the sample b)Co distribution in the sample

In the image showed in 3.9 we can see the distribution of Fe and Co along the sample being the distribution of these compounds simbolized by the yellow and red, respectively.

The distribution of either Fe or Co looks uniform in the whole sample, not appearing any regions with high concentration of one element, (no Fe clusters or Co islands).

This analysis suggests that the sputtering process produced an homogeneous film as desired. Basically, Fe and Co are well mixed and deposited evenly.

3.2.2. X-ray diffraction (XRD)

To determine whether the crystallization of the samples was satisfactory and whether there was no contamination on the samples, we used the X-ray diffraction technique.

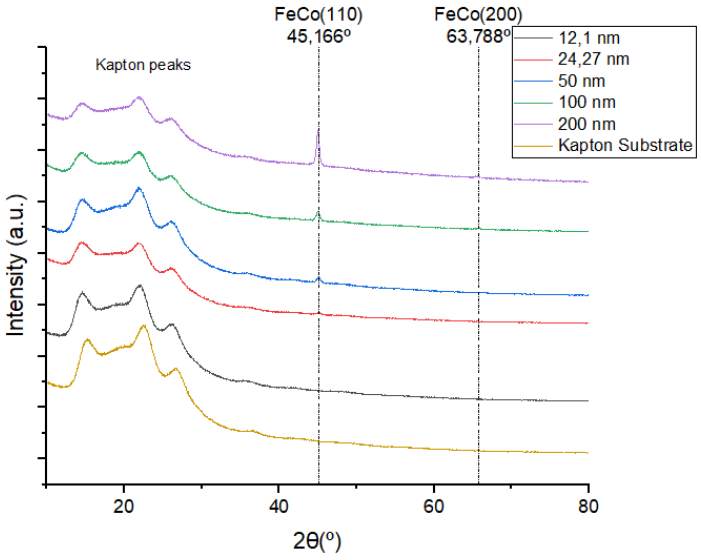

FIGURE 3.10: XRD Image of the samples in kapton substrate

The most prevalent characteristic peaks for FeCo are for $2\theta = 45.166°$ for FeCo(110) and $2\theta = 63.788°$ for FeCo(200), according to materialsproject.org.

It is seen in all of the graphs except for the 12.1 nm one a peak at around $2\theta = 45.166$.

It is possible to identify a few peaks before 40° that also appear in the sample with kapton only spectra, this means those peaks are the peaks of the substrate unrelated to the FeCo sample.

The absence of FeCo peak is assumed to be normal in the graph of the sample with 12.1 nm of material is understandable because of the small amount of material since it is such a small thickness.

As expected, the bigger the amount of FeCo more visible the peaks become.

3.2.3. Magnetic properties

To characterize the magnetic properties of the fabricated samples we used the MPMS.

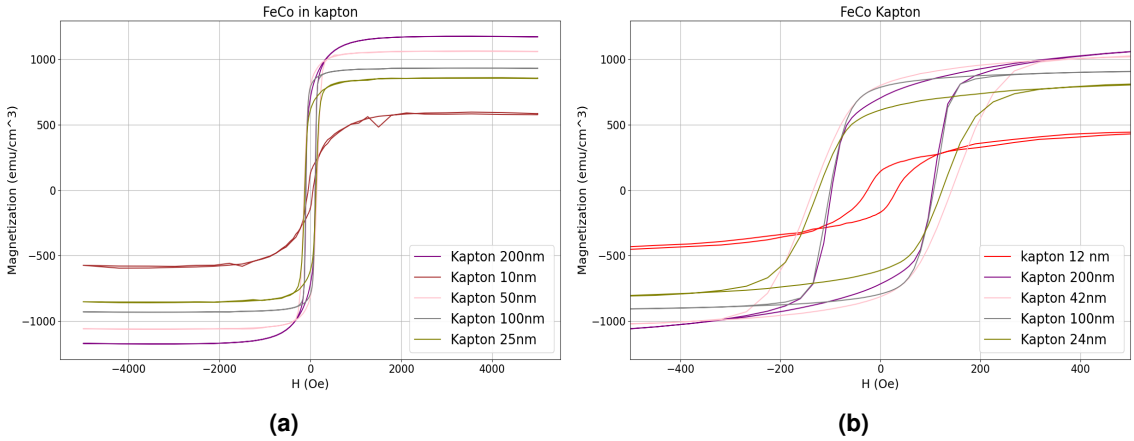

FIGURE 3.11: a)Isothermal M-H of FeCo samples of different thicknesses in Kapton b)is a zoomed in image of a).

We could see the existence of an hysteresis cycle in all of the graphs, showing the ferromagnetic behavior.

As the magnetic field applied in module increases the magnetization increases rapidly until it reaches the maximum where it stabilizes called the magnetization saturation, this happens because the field induces the domains in the material to align until it reaches a maximum where all of them are aligned.

Reducing the applied field to zero does not bring the magnetization to zero, a magnetization remains called remanent magnetization. Cycling H due to this remanent magnetization is what produces the hysteresis loop verified in the graphs.

One particularly interesting observation is the unusual shape of the magnetization curve for the 10 nm sample. However, we were unable to find a definitive answer for this behavior.

All of the other samples exhibited the expected hysteresis cycle, achieving lower coercivity values and sufficiently higher magnetization assuming a successful crystallization of the particles in the sample.

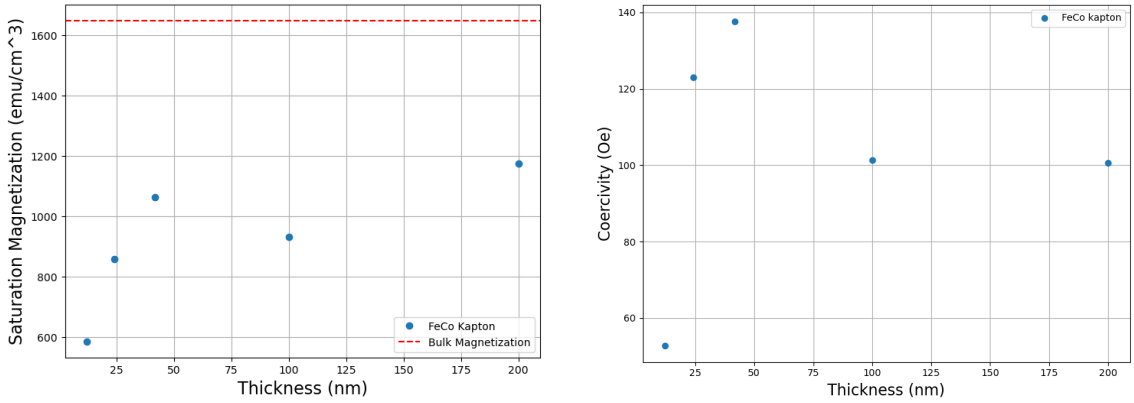

FIGURE 3.12: a) Graph of the saturation magnetization of all the samples measured in the SQUID. b) Graph of the coercivity of all the samples measured in the SQUID.

We see that the magnetization is lower for lower thickness increasing until the 41.74 nm sample, for thicker samples it keeps a similar magnetization. That could be because thinner films still exhibit lower crystallinity of the crystals; however, for thicker films the crystallinity is closer to the maximum amount stabilizing the magnetization saturation.

When comparing FeCo films on flexible Kapton substrates to those on glass, Kapton-supported films generally exhibit higher saturation magnetization, with differences depending on thickness. For the smallest film, Kapton shows a 16.8% higher magnetization than glass. The second thickness shows a slight decrease of 11.9%, indicating that Kapton does not always outperform glass at intermediate sizes. For the third and fourth thicknesses, Kapton demonstrates significant increases of 31.6% and 26.5%, respectively. For the thickest sample, the difference is minimal, with only a 2.3% increase.

These results don't show a clear trend showing that the performance of the FM in kapton can mantain its ferromagnetic characteristics, even achieving bigger saturation magnetization in some of the samples comparing to the glass substrate ones.

It is also possible to be seen that the very thin samples show lower coercivity, that reaches to a maximum for the 41.74 nm sample.The observed size-dependent coercivity in our FeCo samples is consistent with the general trend reported in other magnetic systems[46],[47]. For example in [48] also reported a similar behaviour on $CoFe_2O_4$ refering that they atribute this lowering of coercivity for bigger thiknesses to the transition between single domain to multi-domain magnetic states with the increase in crystal size with the bigger thickness in the samples.

3.2.4. Magnetoresistance

It was measured the magnetoresistivity of the sample with 100 nm of FeCo in order to compare with the future results of FeCo + Bi_2Te_3.

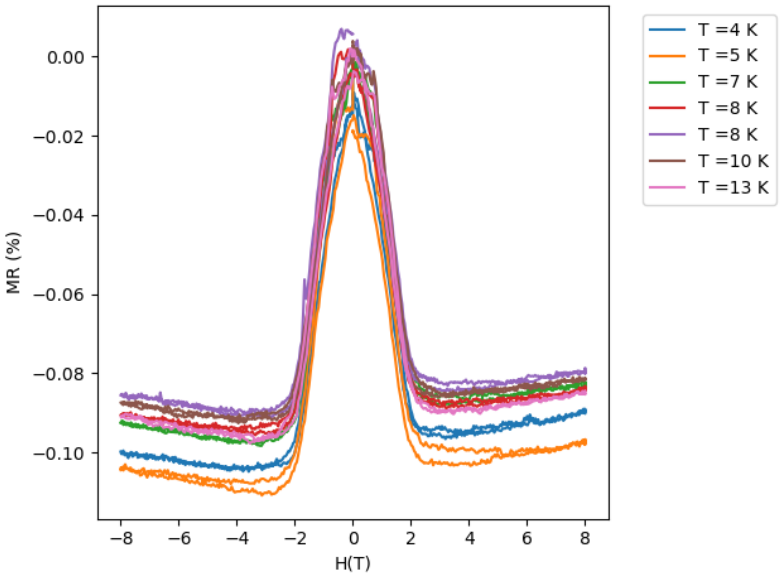

FIGURE 3.13: Magnetoresistance of sample of 100 nm of FeCo

The MR was caluclated using the following formula:

$$MR(H) = \frac{R(H) - R(0)}{R(0)} \times 100\% \tag{3.3}$$

Near zero field domain walls and spin disorder increase scattering causing the reduction of conductivity.

At higher H domain aligns, scattering reduces and conductivity recovers, showing a lower MR.

We see a MR amplitude of 0.8%-0.10% between the temperatures measured

This is consistent with anisotropic magnetoresistance (AMR) and domain switching in a ferromagnet.

4. Heterostructures $FeCo$ + Bi_2Te_3

4.1. Glass substrates

4.1.1. Scanning Electron Microscopy (SEM)/ Energy-Dispersive X-ray Spectroscopy(EDS)

Similarly to the $FeCo$ samples these samples with a topological insulator on top in glass substrate had their surface morphology analyzed by the SEM (Scanning Electron Microscopy), as it is shown in Figure 4.1.

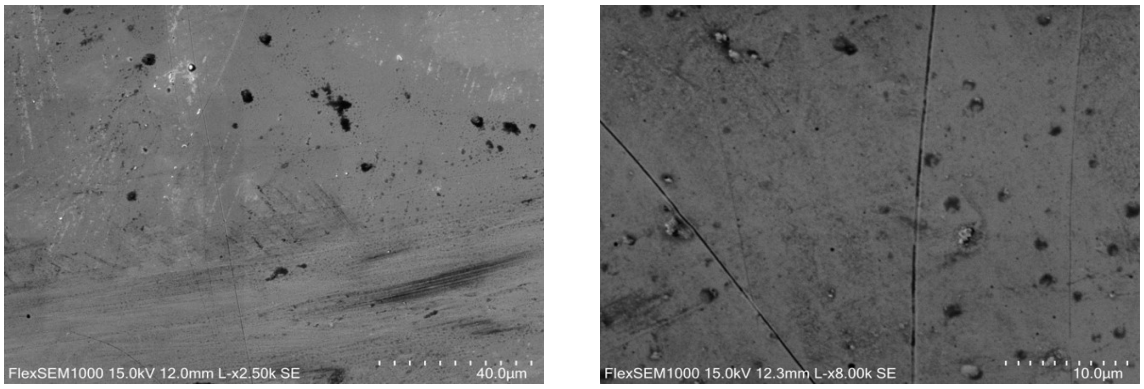

(a) **(b)**

FIGURE 4.1: a)SEM image of the surface of the sample with 100 nm of Bi_2Te_3 on top of 100 nm of $FeCo$ b)SEM image of the surface of the sample with 100 nm of Bi_2Te_3 on top of 50 nm of $FeCo$

We can see in Figure 4.1 that similarly to what is seen in Figure 3.2 the presence of localized dark spots is seen, showing the lack of deposition in certain spots.

It is seen in Figure 4.2 an uniform deposition of the material.

Analyzing Table 4.1, we can see the presence of Fe, Co, Bi and Te in reasonable quantities.

The stoichiometric ratio between Fe:Co should be 1:1 which is very similar to the percentages presented on the table of being the biggest difference on the sample 100M50T with a ratio of 1.17 between Co and Fe. The ratio between Bi and Te should be 2:3 also

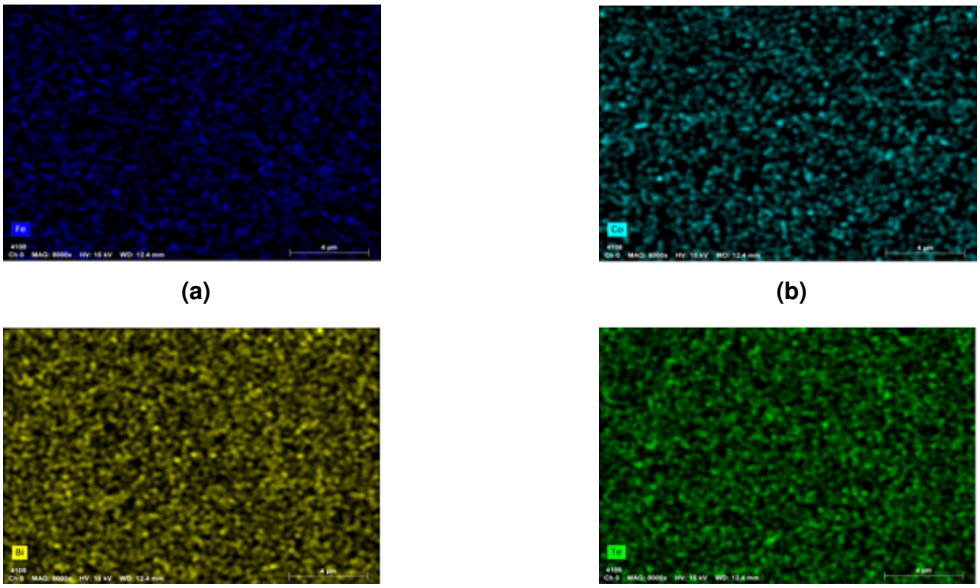

(a) (b) (c) (d)

FIGURE 4.2: a)Fe distribution on the sample of 100 nm of Bi_2Te_3 on top of 50 nm of FeCo b)Co distribution on the sample of 100 nm of Bi_2Te_3 on top of 50 nm of FeCo c)Bi distribution on the sample of 100 nm of Bi_2Te_3 on top of 50 nm of FeCo d)Te distribution on the sample of 100 nm of Bi_2Te_3 on top of 50 nm of FeCo

Sample	Co (Norm.%)	Fe (Norm.%)	Bi (Norm.%)	Te (Norm.%)
100M20T	52.0	44.6	2.9	0.6
100M50T	47.7	40.6	6.0	5.7
100M100T	35.8	33.6	11.5	19.1
25M100T	18.4	17.2	24.7	39.7
50M100T	30.5	26.9	16.1	26.5

TABLE 4.1: Correctly normalized atomic percentages of Co, Fe, Bi, and Te for different samples.

coming in accordance to the percentages that appear on the table for the samples with biggest amount of Bi_2Te_3, however, the other two samples have a smaller amount of Te than Bi, particularly the sample with only 20 nm of topological insulator, what would not be expected. The difference detected in the samples with less Bi_2Te_3 can be atributted to the lower precision for so little amount of material, corroborated by the fact that the error decreases fro bigger thicknesses of Bi_2Te_3.

4.1.2. X-ray Diffraction (XRD)

To understand the crystalization of the samples the X-ray diffraction spectrum was obtained.

We can see in Figure 4.3 the XRD spectrum of the samples with 25 nm of FeCo + 100 nm of Bi_2Te_3 (25M100T on the graph) 50 nm of FeCo + 100 nm of Bi_2Te_3 (50M100T on the graph), 100 nm of FeCo + 100 nm of Bi_2Te_3 (100M100T on the graph),100 nm of FeCo + 20 nm of Bi_2Te_3 (100M20T on the graph) and 100 nm of FeCo + 50 nm of Bi_2Te_3 (100M50T on the graph).

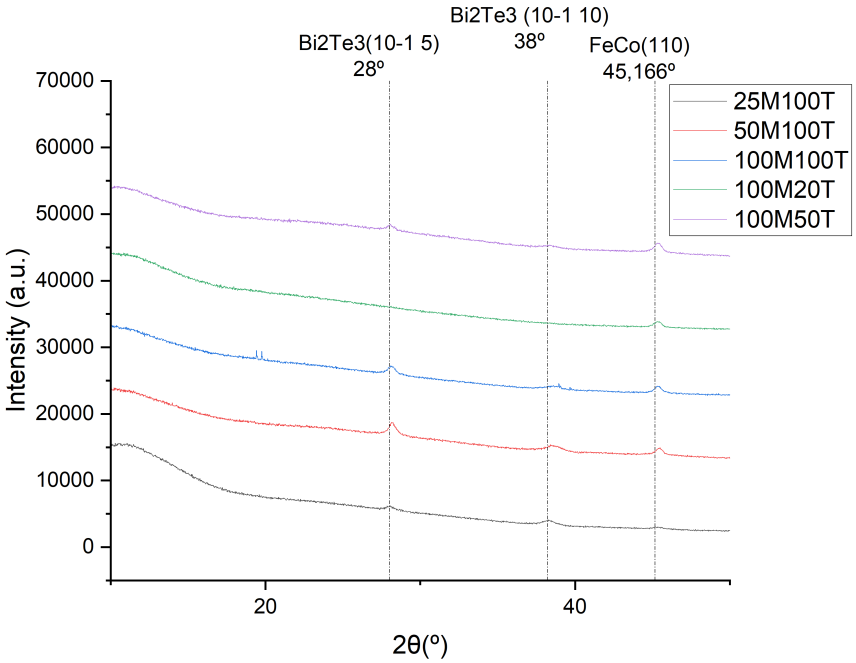

FIGURE 4.3: X-ray Diffraction of $FeCo/Bi_2Te_3$ heterostructures with different thicknesses

We can see in Figure 4.3 the presence of peaks at around 46°, which is smaller for the 25M100T sample. This peak correspond to the FeCo (110) diffraction peak according to materialsproject.org .

It is also possible to see peaks at around 28° and 38° for every samples with exception for the one with only 20 nm of Bi_2Te_3. This is expected since this peaks correspond to the peaks of Bi_2Te_3 (1 0 -1 5) and Bi_2Te_3 (1 0 -1 10), respectively.

From Figure 4.3 we see a successful crystallization and deposition of the sample, being any problems detected in the samples not because of the sample crystallization.

4.1.3. Magnetic Properties

To characterize how the FeCo ferromagnetic characteristics were affected by the topological insulator layer the magnetization response of the sample to an external magnetic field was studied in the SQUID.

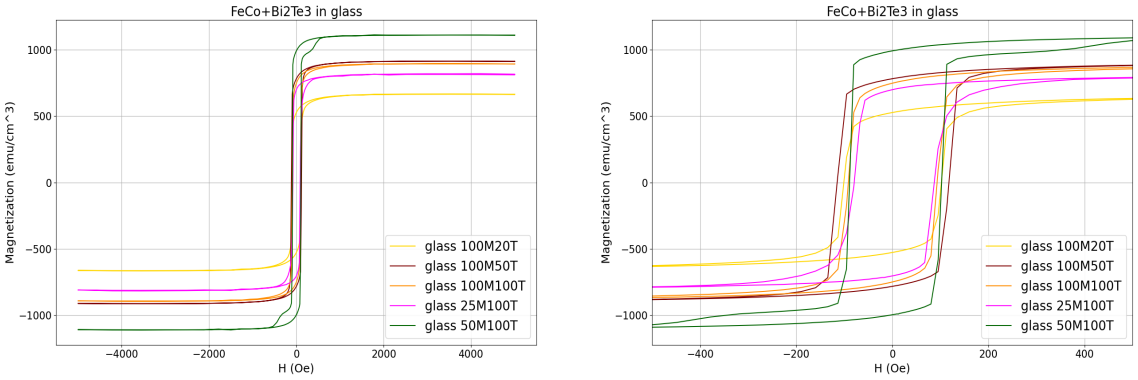

(a) **(b)**

FIGURE 4.4: Isothermal M-H curve of $FeCo/Bi_2Te_3$ samples of different thicknesses

The hysteresis cycle is visible in all of the samples presented in Figure 4.4. This shows that the TI layer does not affect the ferromagnetic behaviour of the sample in these thicknesses.

It is also worth mentioning that the diamagnetic contribution of the plastic straw (sample holder) and of the cotton used to fix the sample, influenced the results.

To correct for this effect, the high-field and low-field regions of the hysteresis curve were analyzed. In this region, the magnetization is saturated and, therefore, any residual slope in the magnetization versus field curve can be attributed to the diamagnetic contributions of the straw and cotton. A linear fit was performed on the saturated portion of the curve, and this fitted slope was then subtracted from the entire dataset.

The graph presented in Figure 4.4 has already been corrected for the background contributions of the sample holder and cotton.

It is possible to see a smaller magnetization saturation for the sample with only 25 nm of $FeCo$, which would already be expected according with the results of the XRD spectrum in Figure 4.3.

Comparing the FeCo/BiTe heterostructures with FeCo-only films of similar thickness shows varied effects depending on the film thickness. For the 100M series, the heterostructures show the following saturation magnetizations: 100M20T = 895 emu/cm³, 100M50T = 810 emu/cm³, and 100M100T = 1107 emu/cm³, whereas the FeCo 100 nm film has 737 emu/cm³. This corresponds to increases of approximately 21.4% for 100M20T, 9.9% for 100M50T, and 50.2% for 100M100T.

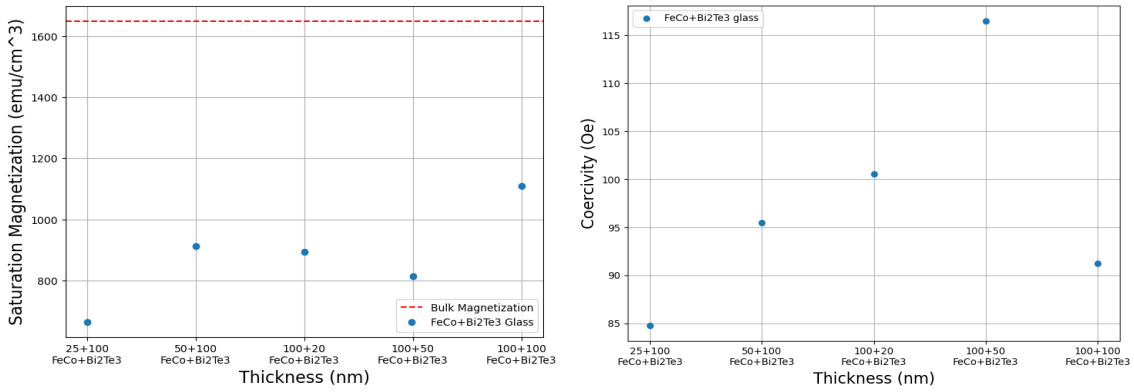

FIGURE 4.5: a)Graph of the saturation magnetization of all the samples measured in the SQUID b)Graph of the coercivity of all the samples measured in the SQUID

Looking at the thinner heterostructures, the 25M100T sample shows a magnetization of 638 emu/cm³, compared to 24.27 nm FeCo film at 973 emu/cm³, reflecting a decrease of 34.4%.

For the 50M100T heterostructure, the magnetization is 912 emu/cm³, compared to 41.74 nm FeCo at 807 emu/cm³, which is an increase of 13%.

Looking at the results it does not look that the Ti can impact negatively magnetization measured.

It is said in [49] that TI next to a ferromagnetic material can influence its ferromagnetic characteristics related to the SOT exchange coupling between the materials.

Looking at both of the graphs in Figure 4.5 it was not decided a clear influence of the Bi_2Te_3 on the magnetic properties of the sample.

4.2. Flexible substrates: Kapton

4.2.1. Scanning Electron Microscopy (SEM) Energy-Dispersive X-ray Spectroscopy(EDS)

To analyze the morphology of these samples these were put through SEM analysis.

In Figure 4.6a it is possible to see a few irregularities in the surface, however they were not considered to be big enough to significantly affect the results.

In Figure 4.6b it is possible to see a the cracks also showed in Figure 3.8. This corroborates the possibility that these cracks appear because of the heating of the substrate

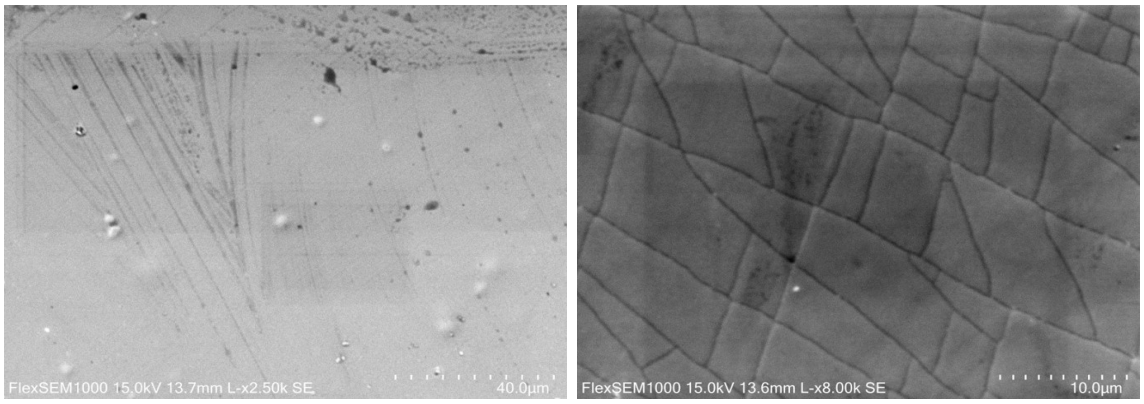

(a) **(b)**

FIGURE 4.6: a)SEM image of the surface morphology of the 25M100T sample on kapton substrate b)SEM image of the surface morphology of the 100M100T sample on kapton substrate

caused by the deposition of FeCo, since the more FeCo is deposited the more cracks it appears.

It was also not seen any dark spots similar to the ones on glass substrate contributing to the idea that the reason for that is coadunated with the substrate. It was also studied the distribution of the materials in the sample to verify if the elements distribution is homogeneous.

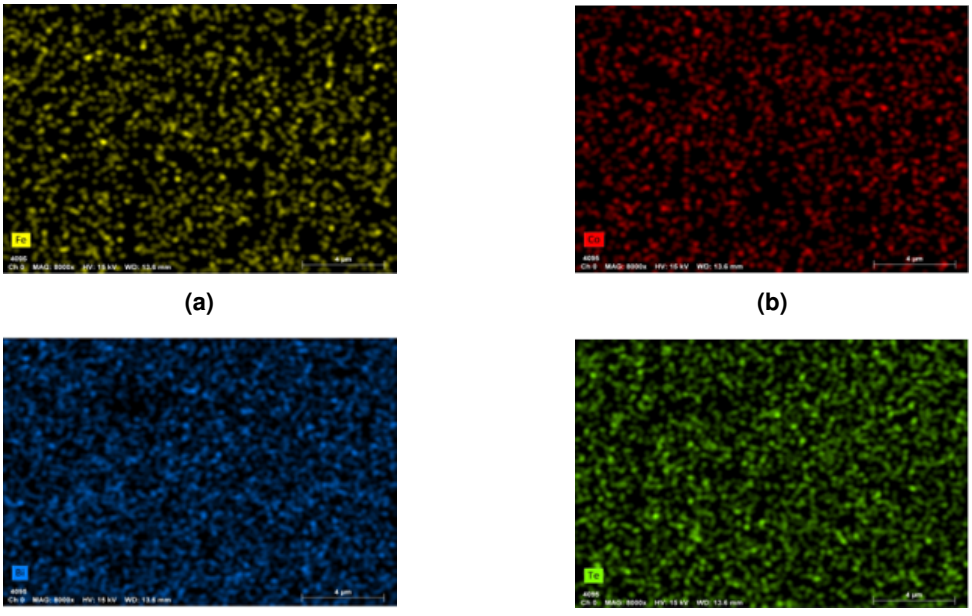

(a) **(b)**

(c) **(d)**

FIGURE 4.7: a)Fe distribution on the sample of 100 nm of Bi_2Te_3 on top of 25 nm of FeCo b)Co distribution on the sample of 100 nm of Bi_2Te_3 on top of 25 nm of FeCo c)Bi distribution on the sample of 100 nm of Bi_2Te_3 on top of 25 nm of FeCo d)Te distribution on the sample of 100 nm of Bi_2Te_3 on top of 25 nm of FeCo

Looking at Figure 4.7 it is not possible to see the formation of any clusters nor any lack of material in any part of the sample.

Sample	Co (Norm.%)	Fe (Norm.%)	Te (Norm.%)	Bi (Norm.%)
100M20T	50.44	42.63	4.92	1.99
100M50T	45.95	39.92	9.87	4.21
100M100T	37.63	32.91	17.03	12.42
25M100T	19.44	18.10	39.42	23.04
50M100T	30.37	26.38	27.76	15.52

TABLE 4.2: Normalized atomic percentages of Co, Fe, Te, and Bi for the samples on kapton substrate.

In the normalized table it is possible to see that Fe:Co have a similar ratio to 1:1 being the biggest difference detected being in the 100M20T with a ratio of 1.19 between Co and Fe, still quite similar to the expected.

The ratio between Bi and Te should be 2:3,similarly to what was seen for the kapton samples that ratio is not followed for the samples 100M20T and 100M50T, however in this case there is a bigger amount of telurium compared to bismuth, while for the glass samples the opposite happened.

This suggests an uneven deposition in those samples.

As for the othern samples the ratio between Te and Bi is around 1.7 in every sample much more similar to the 1.5 value in Bi_2Te_3.

4.2.2. X-ray Diffraction (XRD)

To investigate the crystallization quality of the samples deposited on flexible Kapton substrates, X-ray diffraction (XRD) measurements were performed. This allows us to confirm whether the $FeCo$ and Bi_2Te_3 layers retain the same crystallographic characteristics as the ones observed on glass substrates and to assess if the flexibility of the substrate impacts the crystallinity of the films.

In Figure 4.8 it was shown the X-ray diffraction spectrum of all the samples with $FeCo$ and Bi_2Te_3 in kapton substrate.

The studied samples were 25 nm of $FeCo$ underneath 100 nm of Bi_2Te_3 (referred as 25M100T on the graph) 50 nm of $FeCo$ underneath 100 nm of Bi_2Te_3 (referred as 50M100T on the graph), 100 nm of $FeCo$ underneath 100 nm of Bi_2Te_3 (referred as 100M100T on

the graph),100 nm of $FeCo$ underneath 20 nm of Bi_2Te_3 (referred as 100M20T on the graph) and 100 nm of $FeCo$ underneath 50 nm of Bi_2Te_3 (referred as 100M50T on the graph).

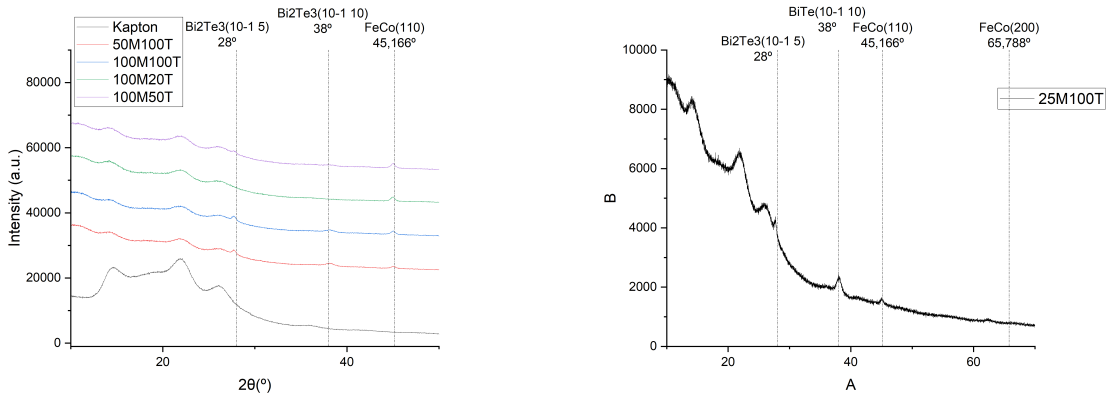

(a) **(b)**

FIGURE 4.8: XRD of the $FeCo/Bi_2Te_3$ heterostructures in kapton substrate

The graph for the sample with 25 nm of $FeCo$ under 100 nm of Bi_2Te_3 was put separately since the measurement conditions were different in that measurement.

It was also put the spectrum of Kapton so it is understood which peaks correspond to the material and which are the caused by the substrate.

It is possible to see peaks (ignoring those because of the kapton) at around 28°, 38° and 48°.

The peak around 48° is less clear for the samples with less FeCo, something to be expected since, it is correspondent to the peak FeCo(110).

The other two peaks correspond to the peaks Bi_2Te_3(1 0 -1 5) and Bi_2Te_3(1 0 -1 10).

These peaks appear only for the samples with 100 nm of Bi_2Te_3 being unindentifiable in the others with less of the material.

4.2.3. Magnetic Properties

To evaluate the effect of the Bi_2Te_3 topological insulator layer on the ferromagnetic properties of the $FeCo$ thin films grown on Kapton substrates, magnetization measurements were performed using the SQUID magnetometer. The analysis of the hysteresis loops

provides information about the magnetic saturation, coercivity, and whether the flexible substrate induces any changes compared to the glass-based samples.

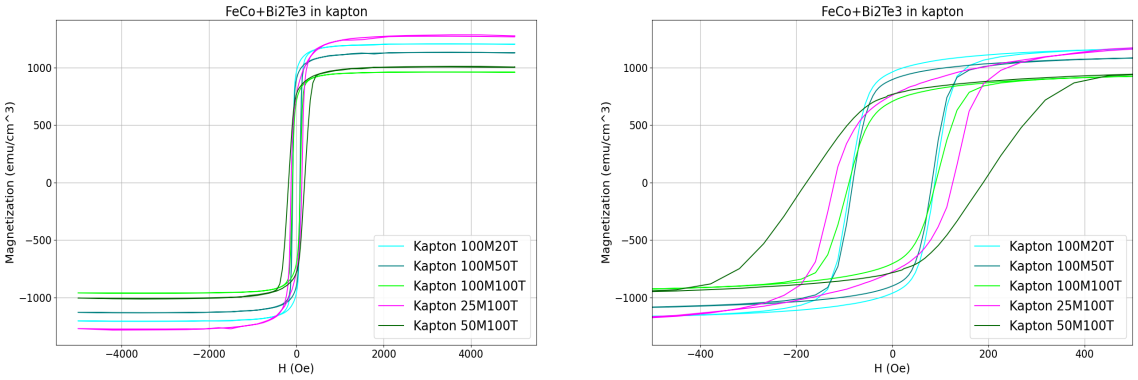

(a) **(b)**

FIGURE 4.9: a) Isothermal M-H curve of $FeCo$ with Bi_2Te_3 on top in kapton substrate of different thicknesses b)Zoomed image of the a).

Similarly to what is seen for the samples in glass, the Bi_2Te_3 layer did not affect the form of the characteristic ferromagnetic hysteresis loop of the sample in the magnetization curve, as we can see in Figure 4.10, not a clear trend was concluded in the samples.

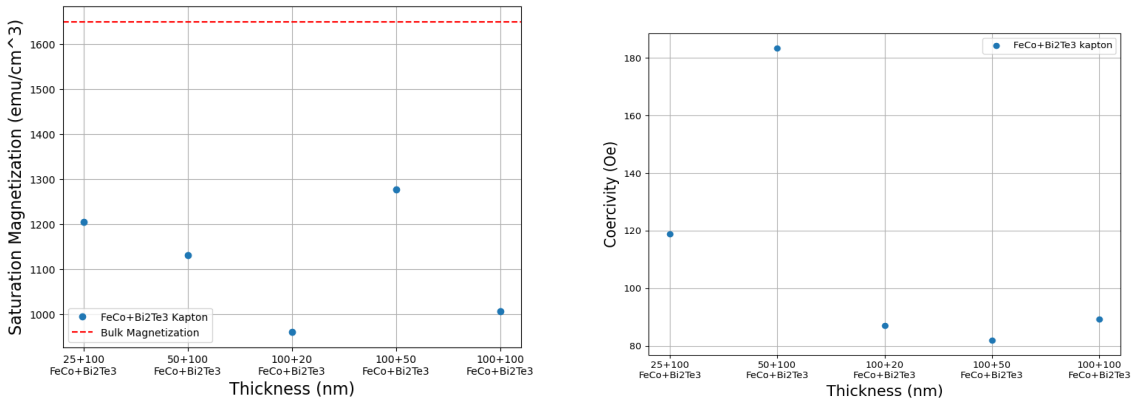

(a) **(b)**

FIGURE 4.10: a)Magnetization saturation of the samples measured in the magnetization curve b)Coercivity of the samples measured in the magnetization curve

Comparing the 100M series heterostructures with the FeCo-only 100 nm film (Ms = 932 emu/cm³) shows the following: 100M20T = 960 emu/cm³, 100M50T = 1279 emu/cm³, and 100M100T = 1107 emu/cm³. The percentage differences relative to FeCo 100 nm are approximately +3.0% for 100M20T, +37.% for 100M50T, and +18.8% for 100M100T.

For the thinner and intermediate heterostructures, 25M100T has a magnetization of 1208 emu/cm³, compared to 24.27 nm FeCo at 857 emu/cm³, corresponding to a significant increase of 41%. For 50M100T, Ms = 1131 emu/cm³, compared to 41.74 nm FeCo at 1062 emu/cm³, which is an increase of 6.5%.

This suggests that the TI does not diminish the measured magnetism of the sample.

4.2.4. Magnetoresistance

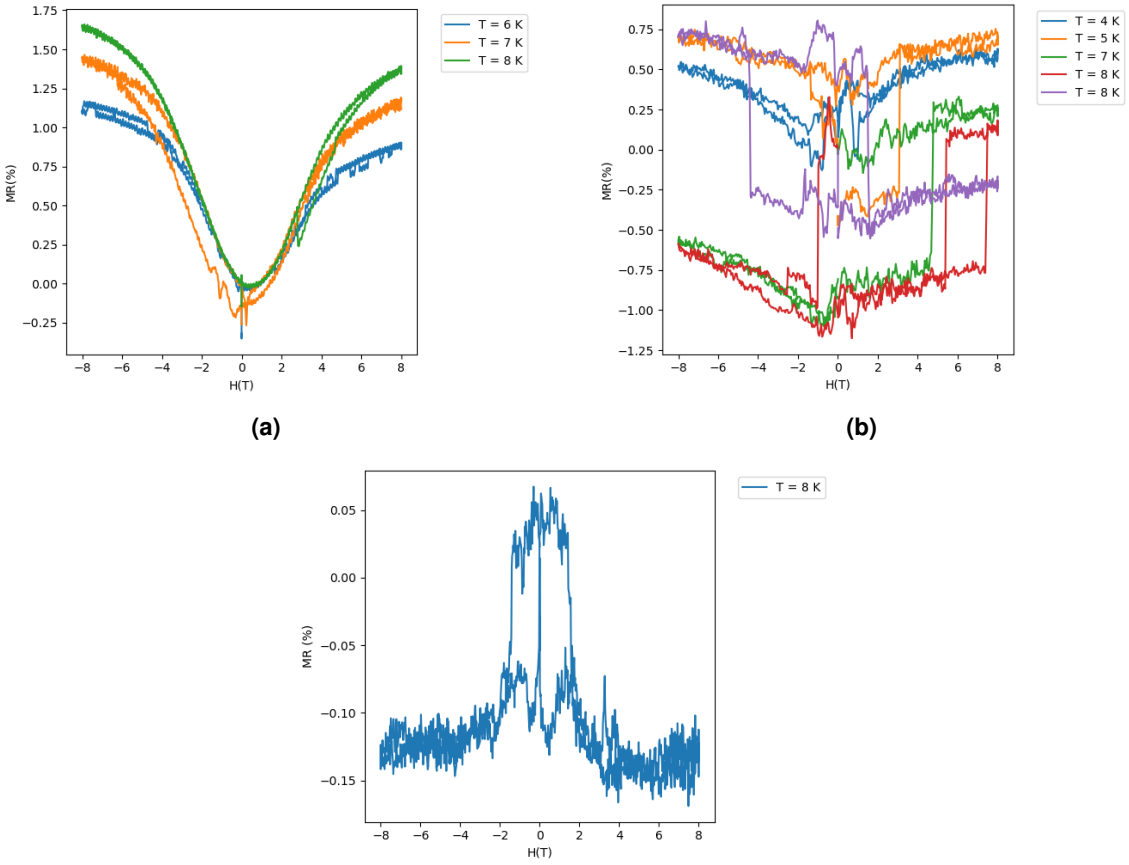

FIGURE 4.11: a)Magnetoresistance graph for some T of the 25M100T sample b)Magnetoresistance graph for some T of the 100M100Tsample c)Magnetoresistance graph for some T of the 100M20T sample

The MR was calculated using Equation 3.3, and was shown the curve for some of the measured temperatures.

The magnetoresistance (MR) results reveal three clearly distinct regimes as a function of the relative thickness and composition of the $FeCo/Bi_2Te_3$ heterostructures. In the sample with the highest TI content , the MR curve exhibits a pronounced weak anti-localization (WAL) signature, characterized by a sharp V-shaped cusp at low magnetic

fields (see Fig.4.11a)[50]. This behavior is consistent with the strong spin–orbit coupling intrinsic to topological insulators and has been widely reported in the literature as a hallmark of quantum interference effects in two-dimensional transport channels. The presence of WAL indicates that in this regime the electrical conduction is dominated by the surface states of the BiTe layer, with the FeCo contribution playing only a minor role due to its relatively reduced effective thickness.

In sharp contrast, the sample containing the thickest magnetic FeCo layer shows an MR curve that resembles more closely the response of a pure magnetic thin film (see Fig. 4.11c). In this case, the significantly lower resistivity of FeCo compared to BiTe leads to the formation of a preferential conduction path through the magnetic layer. As a result, a short-circuit effect occurs, whereby the majority of the applied current bypasses the topological layer and instead flows through the metallic FeCo film. Consequently, the WAL contribution is strongly suppressed, and the MR response becomes governed predominantly by the magnetization processes of FeCo, thus resembling the behavior observed in the standalone magnetic reference film (see Fig. 3.13)[51].

The intermediate configuration presents the most complex MR behavior, with a response that cannot be attributed exclusively to either WAL or magnetic contributions. Instead, the MR curve clearly reveals a coexistence of both effects, reflecting a superposition of the WAL feature from the topological insulator and the negative MR associated with spin-dependent scattering in the magnetic layer (see Fig. 4.11b).[52]

This mixed regime highlights the competition between the two conduction channels and emphasizes the sensitivity of the overall transport properties to the delicate balance between layer thickness, interface quality, and relative conductivity of the heterostructure components.

Taken together, these results demonstrate the potential of FeCo/BiTe heterostructures as a versatile platform for engineering tunable magnetoresistance responses. By carefully controlling the thickness and composition of the layers, it becomes possible to reproducibly access qualitatively different transport regimes, ranging from WAL-dominated conduction to magnetic-layer-dominated behavior, or even hybrid states in which both contributions coexist. Such tunability is not only of fundamental scientific interest but also offers promising perspectives for technological exploitation. In particular, the ability to switch between distinct MR signatures in a controlled manner opens avenues for the design of novel magnetic sensors, spintronic devices, and logic memories where the

interplay between topological and magnetic effects can be harnessed as an additional degree of freedom.

5. Conclusions and future perspectives

The work carried out in this thesis enabled a comprehensive investigation of FeCo thin films and $\mathrm{FeCo/Bi_2Te_3}$ heterostructures, emphasizing the role of substrate type, film thickness, and layer composition on structural, morphological, and magnetic properties. By systematically studying both rigid (glass) and flexible (Kapton) substrates, this work provides insights into how mechanical constraints, thermal expansion, and surface interactions influence film growth, magnetic performance, and overall heterostructure stability. The integration of ferromagnetic FeCo with topological insulators, such as $\mathrm{Bi_2Te_3}$, was shown to be feasible while preserving robust magnetic behavior, which is essential for potential applications in flexible spintronic devices.

For the FeCo-only samples, SEM and XRD analyses confirmed polycrystalline growth with a preferential (110) orientation, consistent with the known crystallographic behavior of FeCo alloys. Structural analysis indicated a strong dependence of microstructure on film thickness: thinner films exhibited granular and partially discontinuous regions, whereas thicker films developed continuous grains with increased surface roughness. Substrate effects were also evident. On glass, minor voids or dark spots were occasionally observed, likely due to incomplete nucleation or local stress during deposition. In contrast, Kapton substrates promoted more uniform coverage, but micro-cracks emerged in thicker films, reflecting the substrate's flexibility and thermal expansion mismatch with the FeCo layer. These microstructural features had a direct influence on magnetic behavior, particularly in dynamic measurements.

Magnetic characterization through SQUID magnetometry revealed robust ferromagnetic behavior across all samples. Saturation magnetization (M_s) values for FeCo on glass ranged from 501 emu/cm³ for the thinnest films to 1.203 emu/cm³ for the thickest, while coercivity (H_c) varied from 52 Oe to 181 Oe, demonstrating the strong intrinsic ferromagnetic character of the FeCo alloy. On Kapton, M_s values spanned from 585 emu/cm³ to 1.219 emu/cm³, with coercivity between 53 Oe and 138 Oe, indicating that flexible substrates can support comparable magnetic properties with only minor modifications due

to mechanical strain. These results confirm that high-purity FeCo ($Fe_{50}Co_{50}$, 99.99%) maintains stable ferromagnetism across thicknesses and substrates, and that substrate effects are largely limited to surface morphology and minor coercivity variations. Ferromagnetic resonance (FMR) measurements, although broadened by polycrystallinity and slight structural inhomogeneities, corroborated the dynamic magnetic response and suggested uniform spin precession across most of the film, with thinner films exhibiting slightly larger linewidths due to enhanced surface-to-volume effects.

The study of $FeCo/Bi_2Te_3$ heterostructures revealed that the deposition of the topological insulator layer preserves the ferromagnetic properties of FeCo while introducing interfacial structural complexity. XRD and XRR measurements confirmed the crystalline nature of both layers, with Bi_2Te_3 showing characteristic diffraction peaks consistent with its layered structure. Magnetic characterization indicated that $FeCo$ retained substantial saturation magnetization and coercivity in heterostructures, with, for example, 100M100T samples exhibiting M_s of 961 emu/cm³ on glass and 893 emu/cm³ on Kapton, and coercivities of 91 Oe and 89 Oe, respectively. These values demonstrate that the presence of Bi_2Te_3 does not significantly degrade the ferromagnetic response, while FMR spectra exhibited broader linewidths, reflecting increased surface roughness, polycrystallinity, and minor structural inhomogeneities at the $FeCo/Bi_2Te_3$ interface. Morphologically, the Bi_2Te_3 layer sometimes mitigated certain surface irregularities of the FeCo film, but also introduced new defects, which may influence spin scattering and magnetic damping.

The interplay between film thickness and substrate type was found to be critical in determining both static and dynamic magnetic properties. Thicker films generally showed higher saturation magnetization due to reduced surface-to-volume ratio effects and more complete grain coalescence, yet Kapton substrates displayed crack formation at higher thicknesses, which could impact film continuity, magnetic uniformity, and device reliability. Interestingly, the coercivity did not scale monotonically with thickness but showed minor fluctuations, reflecting subtle influences of microstructural stress, substrate interaction, and grain boundary density. When comparing FeCo films and $FeCo/Bi_2Te_3$ heterostructures across different substrates, it became evident that glass provided slightly more stable and uniform magnetic behavior, whereas Kapton offered the advantage of flexibility at the expense of some structural irregularities.

Overall, this thesis demonstrates that FeCo thin films maintain strong and stable ferromagnetic properties across a wide range of thicknesses and on both rigid and flexible

substrates. The integration with Bi_2Te_3 preserves magnetic performance while introducing interfacial complexity that may be exploited for spin–orbit coupling phenomena. The combination of robust ferromagnetism, topological insulating behavior, and flexible substrate compatibility establishes $FeCo/Bi_2Te_3$ heterostructures as promising candidates for next-generation spintronic devices, including mechanically flexible or wearable technologies. Furthermore, the results underscore the importance of optimizing deposition parameters, controlling film thickness, and selecting appropriate substrates to minimize defects, maximize crystallinity, and ensure uniform magnetic and structural properties. These findings provide a strong foundation for future work aimed at investigating spin transport, interfacial spin–orbit interactions, and device integration strategies, with the ultimate goal of realizing practical spintronic applications that leverage both the magnetic robustness of FeCo and the topological protection offered by Bi_2Te_3.

In the future, several options can be pursued in order to optimize the structural and magnetic properties of $FeCo/Bi_2Te_3$ heterostructures:

Thermal Treatments and Crystallinity Enhancement, controlled post-deposition thermal annealing could be systematically investigated to improve crystallinity, relieve residual stress, and enhance magnetic uniformity. Such treatments may increase the saturation magnetization and stabilize magnetic performance. Special attention should be paid to flexible substrates such as Kapton, where the low melting temperature poses a fundamental limitation. Innovative annealing protocols (e.g., rapid thermal annealing [53], localized laser annealing [54], or annealing under protective buffer layers [55]) could be explored to overcome this constraint.

Mitigation of Structural Defects in Flexible Films, the tendency of Kapton-based films to develop cracks during post-deposition cooling remains a major challenge. Introducing a thin tantalum (Ta) buffer layer between the substrate and the FeCo layer could serve as an effective thermal and mechanical buffer, mitigating crack formation and enhancing adhesion. Systematic variation of the buffer layer thickness and deposition conditions could help identify optimal architectures for defect suppression.[56]

Interfacial Engineering for Spin–Orbit Effects, since interfacial phenomena govern much of the emergent spintronic behavior, future work should focus on controlling and characterizing the $FeCo/Bi_2Te_3$ interface at the atomic scale.[57]

Advanced growth techniques (e.g., molecular beam epitaxy or pulsed laser deposition under ultrahigh vacuum) combined with in situ surface characterization could enable precise tuning of interfacial structure and chemistry. This would provide a pathway to intentionally engineer interfacial spin–orbit interactions and spin transport efficiency.

Towards Device Integration, beyond fundamental materials optimization, the next logical step is the fabrication of prototype spintronic devices (e.g., spin valves, magnetic tunnel junctions, or spin–orbit torque devices) based on $\mathrm{FeCo/Bi_2Te_3}$ heterostructures.

Integration with flexible platforms will be especially relevant for testing the viability of mechanically deformable or wearable spintronic technologies.

A. Seebeck Coeficient

In order to understand how the material would react to convert thermal energy into electrical energy.

To do this it was connected the two extremities to a multimeter and heating on one of the extremities.

It was not measured the size of the samples since the form factor does not affect the results of these measurements.

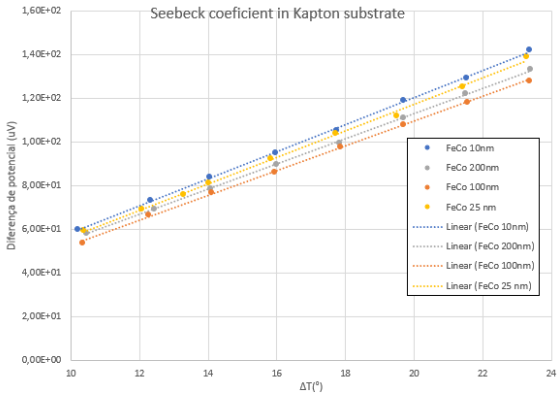

FIGURE A.1: Seeback coeficient calculation of Kapton substrate samples

We can see linear slopes for every thickness indicating the linearity between the difference of temperature and the difference of voltage characteristic of metals.

Looking at the slope of the samples we can clearly see there is a similar slope in every one of them, indicating consistency between the samples, as expected.

It is also possible to see that the fits were made successfully where every fit had at least $r^2 > 0.99$.

B. Annealing

To study the influence of annealing in the magnetization of the samples it was made annealing in vacum in FeCo samples in kapton substrate with thickness 12 nm and 200 nm at 200ºC, 300ºC and 395ºC, doing slow cooling and fast cooling for each sample and for each temperature.

The samples were placed in a quartz tube, conected to a pump used to keep the sample in a vacuum and then the tube was introduced in a oven shown in Figure B.1.

FIGURE B.1: Annealing oven and pump setup

The fast cooling was achieved introducing the quartz tube used in the heating in a bucket with water and ice.

The results were later discarded because no significant improvements were achieved in the magnetization saturation of the samples, so it was assumed the crystallization of the samples without annealing was enough.

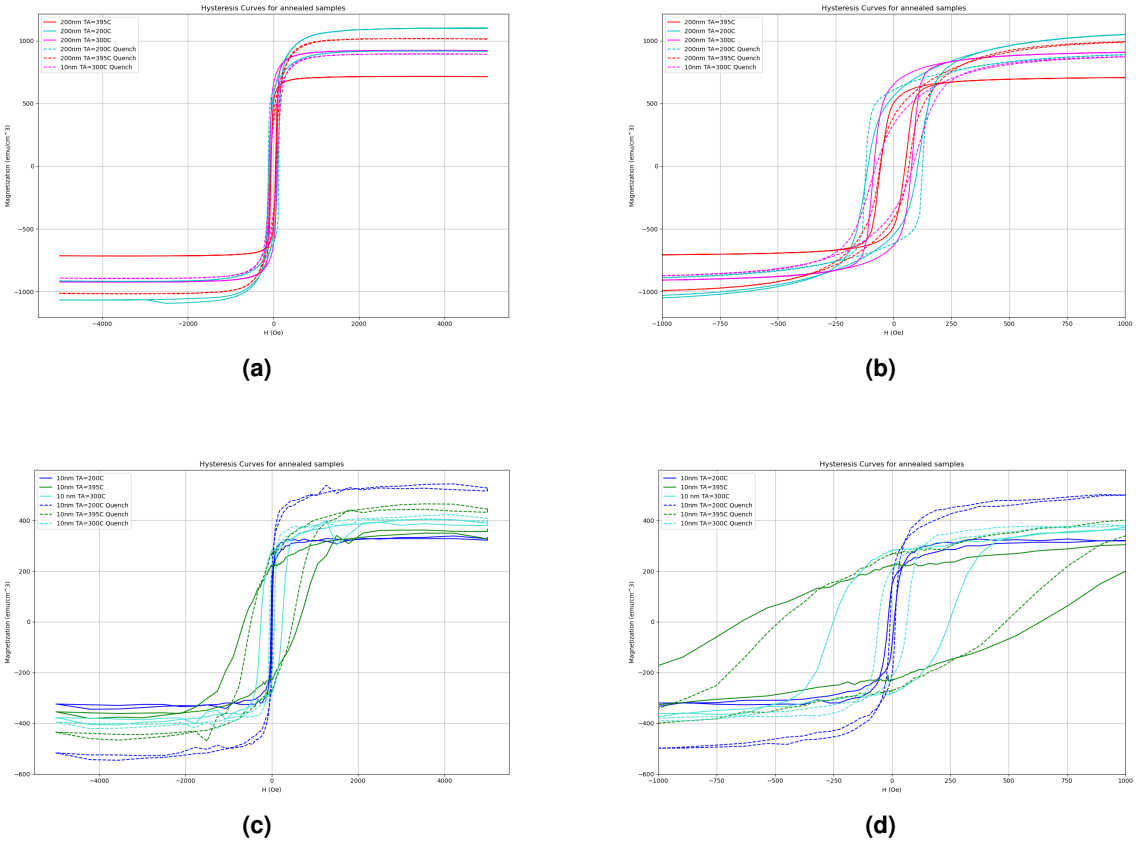

FIGURE B.2: a)Isothermal M-H curve of annealed 200nm samples b)Zoomed image of the hysteresis loop of annealed 200nm samples c)Isothermal M-H curve of annealed 10nm samples d)Zoomed image of the hysteresis loop of annealed 10nm samples

We can clearly see that the magnetization for the 200 nm sample has no significant changes with annealing.

For the 10 nm samples as we can see in B.2c the annealing leads to an increase of magnetization of the sample but nothing really too much significant.

The coercivity appears to reduce with the annealing for the 200 nm sample something already seen in for example [58]. However, for the 10nm samples the opposite happened. This was atributed, likely to polycrystals that can be formed on the sample.

Also, this annealing process was conditioned by the low temperature fusion of the kapton substrate (around 400ºC), since in [59] it is shown that to get a significant improvement on crystalization in the annealing of FeCo samples is necessary to have temperatures higher than at least 370ºC otherwise nothing would be detected.

C. Ferromagnetic Resonance (FMR)

C.1. FMR for $FeCo$ in Flexible substrate (Kapton)

It was also done FMR analysis in these samples. In Figure C.1 are depicted the FMR measurements achieved for the sample with 25 nm thickness.

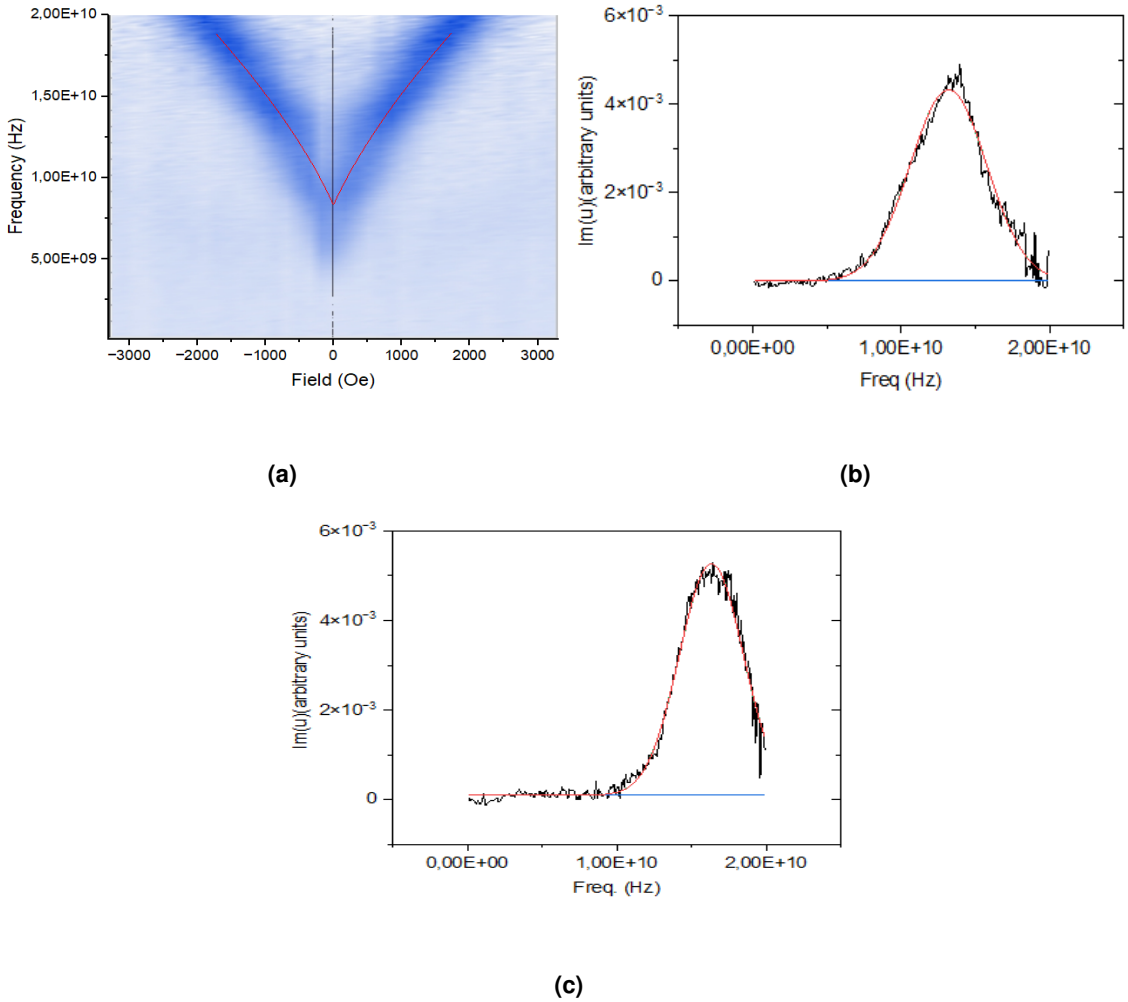

FIGURE C.1: a)Conterplot of resonance frequency for each magnetic field for 25nm of FeCo on kapton substrate b)FMR spectra for 25 nm of FeCo on kapton substrate for an applied field of H=-681.6 Oe c)FMR spectra for 25 nm of FeCo on kapton substrate for an applied field of 1220.95 Oe

In order to extract the resonance frequency from the FMR spectra, Gaussian fits were

applied to the experimental curves whenever possible. The resonance frequency was taken as the peak position of the fitted curve. However for some samples, particularly the thicker films, the FMR spectra displayed complex features taht could not be reliably fitted with the Gaussian model.

Attempts were also made to calculate the damping parameter using the linewidth of the resonance peaks. Nevertheless, this approach was not successful. In many spectra, the linewidths were either excessively broad or poorly defined, preventing accurate fitting. Since the damping is intrinsically small, even small uncertainties in the linewidth introduce large errors, making it impossible to extract meaningful damping values from these measurements.

The pronounced peak broadening observed in several spectra can be attributed to microstructural inhomogeneities within the films. The presence of microparticles in the deposited layers can give rise to additional scattering mechanisms, such as magnon scattering, which directly contribute to the increase in linewidth.Furthermore, the detection of multiple peaks in certain spectra suggests the existence of nanocrystal clusters or regions with random crystal orientation, both of which can induce variations in the local magnetic environment and result in complex resonance responses.[60]

Overall, while the FeCo films on Kapton substrates clearly exhibit ferromagnetic resonance, the spectral quality is strongly influenced by film morphology and structural defects. This highlights the importance of optimizing deposition conditions and substrate preparation in order to improve the homogeneity of the films and to enable a more accurate determination of dynamic magnetic parameters such as damping.

It was also used Equation 3.2 to fit the anisotropy field and the magnetization saturation in Table C.1

Sample Thickness (nm)	**Ha (Oe)**	**Ms (emu/cm^3)**
12.1	18 ± 40	853 ± 13
24.27	-13 ± 30	1469 ± 29
41.74	No information	No information
100	No information	No information
200	-17 ± 46	1278 ± 170

TABLE C.1: Magnetic anisotropy field (H_a) and magnetization saturation (Ms) for different sample thicknesses.

C.2. FMR in heterostructure $FeCo/Bi_2Te_3$

C.2.1. Glass substrate

After establishing the static magnetic properties of the sample, it is also important to probe the dynamic magnetic behavior. To achieve this, ferromagnetic resonance (FMR) measurements were carried out.

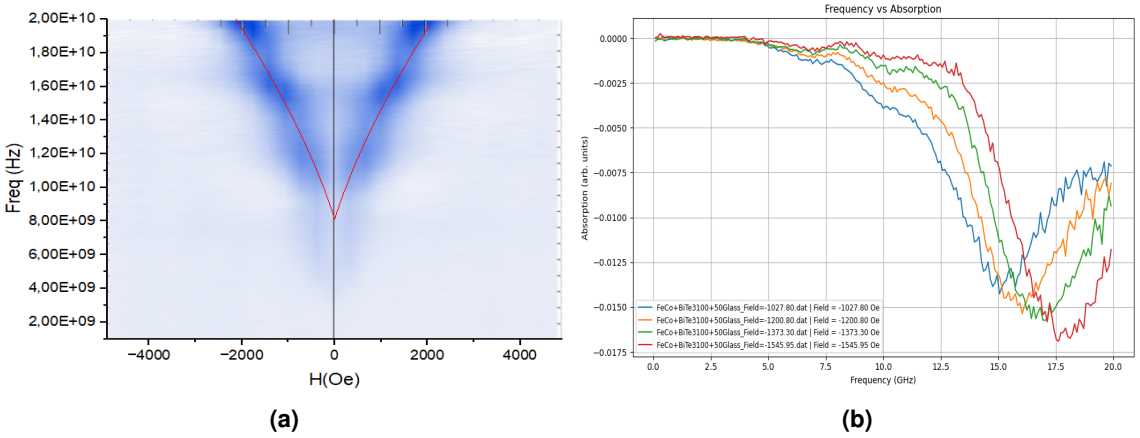

FIGURE C.2: a)Kittel fit of FMR conterplot of the sample of 20nm of Bi_2Te_3 on top of 100 nm of $FeCo$ in glass substrate b)FMR spectra for some different fields for the sample of 50nm of Bi_2Te_3 on top of 100 nm of $FeCo$ in glass substrate

We can see on Figure C.2b the complexity and broadening of the FMR curves that would lead to a dificult analyzis and the impossibility of the damping calculation just like the examples in the chapters before.

There were obtained worse curves in these samples, reason being that the samples thickness being bigger for smaller ferromagnetic material.

It was also seen very little anisotropy field in all the fits showing a non-preferencial orientation of the crystals in the films, as seen on Table C.2

Sample	Ha (Oe)	Ms (emu/cm^3)
100M20T	-11 ± 53	1348 ± 146
100M50T	-59 ± 49	1033 ± 128
100M100T	No information	No information
25M100T	156 ± 92	1273 ± 173
50M100T	No information	No information

TABLE C.2: Magnetic anisotropy field (H_a) and Magnetization saturation (Ms) for different different samples of $FeCo$ with Bi_2Te_3.

C.2.2. Flexible substrate: Kapton

In addition to the static magnetic characterization, the dynamic magnetic behavior of the Kapton-based samples was investigated through ferromagnetic resonance (FMR) measurements. This technique allows the study of magnetic damping and anisotropy, and it is particularly useful to verify if the flexible substrate influences the linewidth or the resonance field of the films.

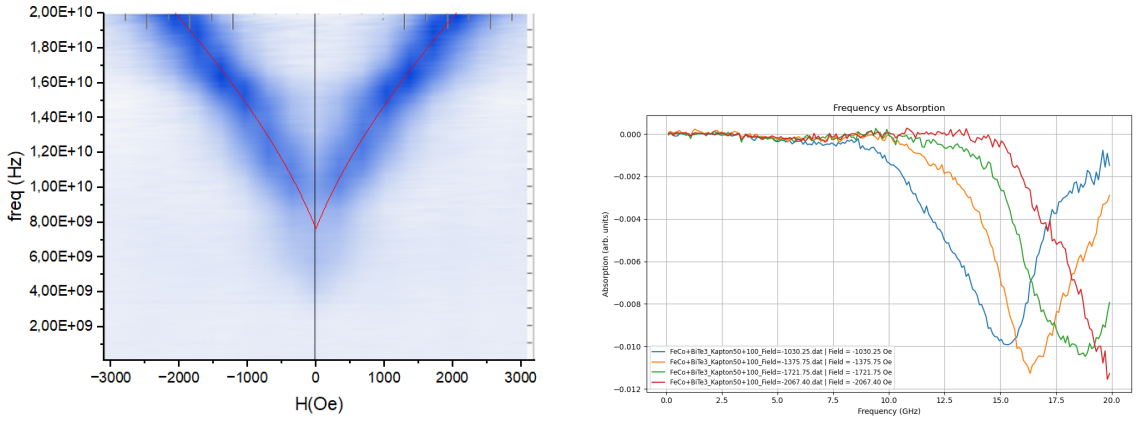

(a) **(b)**

FIGURE C.3: a)Counterplot of resonance frequency for each magnetic field with Kittel fit included for sample 50 nm of $FeCo$ and 100 nm of Bi_2Te_3 b)FMR spectra for different applied fields for the sample of 100nm $FeCo$ and 50nm Bi_2Te_3

The results continue to be very similar to the glass substrate samples, the damping is impossible to calculte due to the bigger broadening of the peaks.

Just like the others it was not detected a big anisotropy field in any sample showing no any preference in the orientation of the crystals, as seen in Table C.3

Sample	Ha (Oe)	Ms (emu/cm^3)
100M20T	-25 ± 31	856 ± 37
100M50T	No information	
100M100T	No information	
25M100T	-65 ± 5	1671 ± 58
50M100T	-39 ± 44	1460 ± 189

TABLE C.3: Magnetic anisotropy field (H_a) and Magnetization saturation (Ms) for the different samples in kapton substrate.

Bibliography

[1] M. Z. Hasan and C. L. Kane. Colloquium: Topological insulators. *Rev. Mod. Phys.*, 82:3045–3067, Nov 2010. [Cited on pages xi, 1, and 2.]

[2] Xiao-Liang Qi and Shou-Cheng Zhang. Topological insulators and superconductors. *Rev. Mod. Phys.*, 83:1057–1110, Oct 2011. [Cited on page 1.]

[3] Ching-Kai Chiu, Jeffrey C. Y. Teo, Andreas P. Schnyder, and Shinsei Ryu. Classification of topological quantum matter with symmetries. *Rev. Mod. Phys.*, 88:035005, Aug 2016. [Cited on pages 1 and 2.]

[4] Pranab Kumar Das, Jagoda Sławińska, Ivana Vobornik, Jun Fujii, Anna Regoutz, Juhan M. Kahk, David O. Scanlon, Benjamin J. Morgan, Cormac McGuinness, Evgeny Plekhanov, Domenico Di Sante, Ying-Sheng Huang, Ruei-San Chen, Giorgio Rossi, Silvia Picozzi, William R. Branford, Giancarlo Panaccione, and David J. Payne. Role of spin-orbit coupling in the electronic structure of IrO_2. *Physical Review Materials*, 2(6):065001, 2018. [Cited on pages xi and 2.]

[5] Dianjohn Hsieh, Yiman Xia, Dong Qian, L. Wray, Hugo Dil, Fabian Meier, J Osterwalder, Luc Patthey, J Checkelsky, Phuan Ong, Alexei Fedorov, Hsiu-Hau Lin, A Bansil, D Grauer, YS Hor, R Cava, and M. Zahid Hasan. A tunable topological insulator in the spin helical dirac transport regime. *Nature*, 460:1101–5, 08 2009. [Cited on pages xi and 2.]

[6] Wenchao Ma, Raphaël Pestourie, and Steven G. Johnson. Time-reversal-symmetry bounds on electromagnetic fields. *Phys. Rev. A*, 111:063518, Jun 2025. [Cited on page 3.]

[7] Berthold Jäck, Yonglong Xie, B. Andrei Bernevig, and Ali Yazdani. Observation of backscattering induced by magnetism in a topological edge state. *Proceedings of the National Academy of Sciences*, 117(28):16214–16218, June 2020. [Cited on page 3.]

[8] Tengfei Zhang, Shenjin Wei, Xiaoxiao Song, Shubo Zhang, Yaopeng li, Yiyun Zou, Ying Wang, Menghan Li, Ying Jiang, Junhua Wang, Hu Ertao, and Jing Li. Annealing effect on linear and ultrafast nonlinear optical properties of bi2te3 thin films. *Materials*, 17:6281, 12 2024. [Cited on page 4.]

[9] Mengyun He, Huimin Sun, and Qing He. Topological insulator: Spintronics and quantum computations. *Frontiers of Physics*, 14:43401, 05 2019. [Cited on pages 4 and 6.]

[10] M.S. Shalaby, N.M. Yousif, L.A. Wahab, and H.M. Hashem. Structural, optical, and physical properties investigations of bi2te3 topological insulator nanocomposites exposure to 60co -rays. *Materials Science and Engineering: B*, 271:115246, 2021. [Cited on page 4.]

[11] Gregory Stephen, Owen Vail, Jiwei Lu, William Beck, Patrick Taylor, and Adam Friedman. Weak antilocalization and anisotropic magnetoresistance as a probe of surface states in topological bi2texse3x thin films. *Scientific Reports*, 10, 03 2020. [Cited on page 4.]

[12] Zhen Gao, Fei Gao, Youming Zhang, Yu Luo, and Baile Zhang. Flexible photonic topological insulator. *Advanced Optical Materials*, 6:1800532, 06 2018. [Cited on page 4.]

[13] Kohei Hamaya and Michihiro Yamada. Semiconductor spintronics with co2-heusler compounds. *MRS Bulletin*, 47, 07 2022. [Cited on pages xi and 5.]

[14] P. Laczkowski, M. Cosset-Cheneau, W. Savero-Torres, V. T. Pham, G. Zahnd, H. Jaffrès, N. Reyren, J.-C. Rojas-Sànchez, A. Marty, L. Vila, J.-M. George, and J.-P. Attané. Spin-dependent transport characterization in metallic lateral spin valves using one-dimensional and three-dimensional modeling. *Phys. Rev. B*, 99:134436, Apr 2019. [Cited on page 5.]

[15] Yuliang Chen, Kartik Samanta, Naafis Shahed, Haojie Zhang, Chi Fang, Arthur Ernst, Evgeny Tsymbal, and Stuart Parkin. Twist-assisted all-antiferromagnetic tunnel junction in the atomic limit. *Nature*, 632:1–7, 08 2024. [Cited on page 6.]

[16] Yi Wang and Hyunsoo Yang. Spin–orbit torques based on topological materials. *Accounts of Materials Research*, 3, 09 2022. [Cited on page 6.]

[17] Yu-Qing Zhao, Hai-Yan Zuo, Shao-Wei Li, Ke Xia, Ming Wen, Jun-Mei Guo, Peng Xiong, and Cong Ren. Tunneling barrier thickness dependence of spin polarization of ferromagnet in magnetic tunnel junctions. *Chin. Phys. Lett.*, 41(11):117201, 2024. [Cited on page 7.]

[18] Dr. Arvind Kumar, Pawan Singh, Mohd Sadiq, and Rishi Singh. A first principle study of magnetic and opto-electronic properties of half metallic heusler alloy, co2tisi. *Materials Today: Proceedings*, 47, 05 2021. [Cited on page 7.]

[19] Jack Bass and William P Pratt. Spin-diffusion lengths in metals and alloys, and spin-flipping at metal/metal interfaces: an experimentalist's critical review. *Journal of Physics: Condensed Matter*, 19(18):183201, April 2007. [Cited on page 7.]

[20] F. J. Jedema, M. S. Nijboer, A. T. Filip, and B. J. van Wees. Spin injection and spin accumulation in all-metal mesoscopic spin valves. *Physical Review B*, 67(8), February 2003. [Cited on page 8.]

[21] M. Creff, F. Faisant, J. Rubi, and J.-E Wegrowe. Surface currents in hall devices. *Journal of Applied Physics*, 128:054501, 08 2020. [Cited on pages xi and 8.]

[22] Naoto Nagaosa, Jairo Sinova, Shigeki Onoda, A. H. MacDonald, and N. P. Ong. Anomalous hall effect. *Rev. Mod. Phys.*, 82:1539–1592, May 2010. [Cited on page 9.]

[23] Martin Obstbaum. Inverse spin hall effect in metallic heterostructures. *arxiv*, 2016. [Cited on page 9.]

[24] Xinde Tao, Qi Liu, Bingfeng Miao, Rui Yu, Zheng Feng, Liang Sun, Biao You, Jun Du, Kai Chen, Shufeng Zhang, Luo Zhang, Zhe Yuan, di wu, and H. F. Ding. Self-consistent determination of spin hall angle and spin diffusion length in pt and pd: The role of the interface spin loss. *Science Advances*, 4:eaat1670, 06 2018. [Cited on page 10.]

[25] Jairo Sinova, Sergio O. Valenzuela, J. Wunderlich, C. H. Back, and T. Jungwirth. Spin hall effects. *Rev. Mod. Phys.*, 87:1213–1260, Oct 2015. [Cited on pages 10 and 11.]

[26] Thomas K. Reid, S. Pamir Alpay, Alexander V. Balatsky, and Sanjeev K. Nayak. First-principles modeling of binary layered topological insulators: Structural optimization

and exchange-correlation functionals. *Phys. Rev. B*, 101:085140, Feb 2020. [Cited on page 10.]

[27] S. Miyakoshi and Yukinori Ohta. Antiferromagnetic topological insulator state in the correlated bernevig-hughes-zhang model. *Physical Review B*, 87, 04 2013. [Cited on pages xi and 11.]

[28] Y. L. Chen, J. G. Analytis, J.-H. Chu, Z. K. Liu, S.-K. Mo, X. L. Qi, H. J. Zhang, D. H. Lu, X. Dai, Z. Fang, S. C. Zhang, I. R. Fisher, Z. Hussain, and Z.-X. Shen. Experimental realization of a three-dimensional topological insulator, bi2te3. *Science*, 325(5937):178–181, 2009. [Cited on page 12.]

[29] Yusheng Hou, Jeongwoo Kim, and Ruqian Wu. Magnetizing topological surface states of bi¡sub¿2¡/sub¿se¡sub¿3¡/sub¿ with a cri¡sub¿3¡/sub¿ monolayer. *Science Advances*, 5(5):eaaw1874, 2019. [Cited on page 12.]

[30] Chaoxing Liu and Shoucheng Zhang. Chapter 3 - models and materials for topological insulators. In Marcel Franz and Laurens Molenkamp, editors, *Topological Insulators*, volume 6 of *Contemporary Concepts of Condensed Matter Science*, pages 59–89. Elsevier, 2013. [Cited on page 12.]

[31] Timothy H. Hsieh, Hsin Lin, Junwei Liu, Wenhui Duan, Arun Bansil, and Liang Fu. Topological crystalline insulators in the snte material class. *Nature Communications*, 3(1), July 2012. [Cited on page 12.]

[32] B. Andrei Bernevig, Taylor L. Hughes, and Shou-Cheng Zhang. Quantum spin hall effect and topological phase transition in hgte quantum wells. *Science*, 314(5806):1757–1761, 2006. [Cited on page 12.]

[33] T. Vemulkar, R. Mansell, A. Fernández-Pacheco, and R. P. Cowburn. Toward flexible spintronics: Perpendicularly magnetized synthetic antiferromagnetic thin films and nanowires on polyimide substrates. *Advanced Functional Materials*, 26(26):4704–4711, 2016. [Cited on page 12.]

[34] G. PRADHAN, F. CELEGATO, G. BARRERA, E.S. OLIVETTI, M. COISSON, J. HAJDUČEK, J. ARREGI URIBEETXEBARRIA, L. ČELKO, V. UHLÍŘ, P. RIZZI, and P. TIBERTO. Magnetic properties of fega/kapton for flexible electronics. *Scientific Reports*, 12(1):11, 2022. [Cited on page 12.]

[35] Marco Cen-Puc, Andreas Schander, Minerva G. Vargas Gleason, and Walter Lang. An assessment of surface treatments for adhesion of polyimide thin films. *Polymers*, 13(1955), 2021. [Cited on page 16.]

[36] Xu Dong Huang, Sunil Madhukar Bhangale, Peter M Moran, Nikolai L Yakovlev, and Jisheng Pan. Surface modification studies of kapton hn polyimide films. *Polym Int*, 52:1064–1069, 2003. [Cited on page 16.]

[37] P. Poulopoulos, S. Grammatikopoulos, D. Trachylis, G. Bissas, I. Dragatsikas, M.J. Velgakis, and C. Politis. Growth and Optical Properties of Nanocrystalline Titania Films for Optoelectronics and Photovoltaics. *Journal of Surfaces and Interfaces of Materials*, 3:52–59, 2015. [Cited on page 22.]

[38] Sofia Ferreira-Teixeira, Alexander Vanstone, Ana L. Pires, Will R. Branford, Joao P. Araujo, Lesley F. Cohen, and Andre M. Pereira. Electronic conduction channels engineered in topological insulator sputtered thin films. *ACS Appl. Electron. Mater.*, 4:5789–5798, 2022. [Cited on page 22.]

[39] Paul J.D. Whiteside, Jeffrey A. Chininis, and Heather K. Hunt. Techniques and challenges for characterizing metal thin films with applications in photonics. *Coatings*, 6, 2016. [Cited on page 22.]

[40] Joana Silva and André Miguel Pereira. Advanced magnetostrictive device for non-destructive testing of critical assets. Master's thesis, Universidade do Porto, Porto, Portugal, 2023. PQDT - Global, Accessed 29 Sept. 2025. [Cited on page 26.]

[41] Wenjie Yang, Junjie Liu, Xiangfeng Yu, Gang Wang, Zhigang Zheng, Jianping Guo, Deyang Chen, Zhaoguo Qiu, and Dechang Zeng. The preparation of high saturation magnetization and low coercivity feco soft magnetic thin films via controlling the thickness and deposition temperature. *Materials*, 15(20), 2022. [Cited on page 27.]

[42] Garima Vashisht, Rajan Goyal, and Annapoorni Subramanian. Exchange stiffness variation for thermally annealed feco thin films. *AIP Conference Proceedings*, 1942:130017, 04 2018. [Cited on page 27.]

[43] Victor Haspot, Paul Noël, Jean-Philippe Attané, Laurent Vila, Manuel Bibes, Abdelmadjid Anane, and Agnès Barthélémy. Temperature dependence of the gilbert damping of $\mathrm{la_{0.7}sr_{0.3}mno_3}$ thin films. *Phys. Rev. Mater.*, 6:024406, Feb 2022. [Cited on page 29.]

[44] M. Madami, S. Tacchi, G. Gubbiotti, G. Carlotti, and G. Socino. Thickness dependence of magnetic anisotropy in ultrathin co/gaas(001) films. *Surface Science*, 566-568:246–251, 2004. Proceedings of the 22nd European Conference on Surface Science. [Cited on page 29.]

[45] E. M. F. Vieira, A. L. Pires, J. P. B. Silva, V. H. Magalhães, J. Grilo, F. P. Brito, M. F. Silva, A. M. Pereira, and L. M. Goncalves. High-performance -thermoelectric device based on bi2te3/sb2te3 p–n junctions. *ACS Applied Materials & Interfaces*, 11(42):38946–38954, 2019. PMID: 31560510. [Cited on page 31.]

[46] Shuang Wu, Kyotaro Abe, Takuma Nakano, Tim Mewes, Claudia Mewes, G. J. Mankey, and Takao Suzuki. Thickness dependence of dynamic magnetic properties of soft (feco)-si alloy thin films. *Physical Review B*, 99, 2019. [Cited on page 35.]

[47] Wenjie Yang andJunjie Liu, Xiangfeng Yu, Gang Wang, Zhigang Zheng, Jianping Guo, Deyang Chen, Zhaoguo Qiu, and Dechang Zeng. The preparation of high saturation magnetization and low coercivity feco soft magnetic thin films via controlling the thickness and deposition temperature. *Materials*, 15, 2022. [Cited on page 35.]

[48] Yue Zhanga, Zhi Yangb, Ben-Peng Zhua, Wei Yuc, Shi Chena, Xiao-Fei Yanga, Fang Jind, and Jun Ou-Yang. Change in the coercivity of $CoFe_2O_4$ nano-particles verified to result from a change in their domain structurer. *Ceramics International*, 40:3439–3443, 2014. [Cited on page 35.]

[49] Peng Wei, Ferhat Katmis, Badih A. Assaf, Hadar Steinberg, Pablo Jarillo-Herrero, Donald Heiman, and Jagadeesh S. Moodera. Exchange-coupling-induced symmetry breaking in topological insulators. *Physical Review Letters*, 110, 2013. [Cited on page 41.]

[50] G. M. Stephen, O. A. Vail, J. Lu, W. A. Beck, P. J. Taylor, and A. L. Friedman. Weak antilocalization and anisotropic magnetoresistance as a probe of surface states in topological $bi_2te_xse_{3-x}$ thin films. *Scientific Reports*, 10(1):4845, March 2020. [Cited on page 47.]

[51] Lalit Pandey, Rahul Gupta, Amir Khan, Nanhe Gupta, Soumyarup Hait, Nakul Kumar, Vireshwar Mishra, Nikita Sharma, Peter Svedlindh, and Sujeet Chaudhary. Topological surface state induced spin pumping in sputtered topological insulator (bi2te3)–ferromagnet (co60fe20b20) heterostructures. *Journal of Applied Physics*, 134, 07 2023. [Cited on page 47.]

[52] Hong-Tao He, Gan Wang, Tao Zhang, Iam-Keong Sou, George K. L Wong, Jian-Nong Wang, Hai-Zhou Lu, Shun-Qing Shen, and Fu-Chun Zhang. Impurity effect on weak antilocalization in the topological insulator. *Physical Review Letters*, 106(16), April 2011. [Cited on page 47.]

[53] Min Young Choi, Dong Joo Choi, Key-One Ahn, Insoo Ro, Young-Ho Kim, and Sang-Hee Suh. Fabrication of copper nanoparticles in a thick polyimide film cured by rapid thermal annealing. *Journal of Nanoscience and Nanotechnology*, 12(4):3637–3640, 2012. [Cited on page 51.]

[54] Francisco J. Romero, Alfonso Salinas-Castillo, Almudena Rivadeneyra, Andreas Albrecht, Andres Godoy, Diego P. Morales, and Noel Rodriguez. In-depth study of laser diode ablation of kapton polyimide for flexible conductive substrates. *Nanomaterials*, 8(7), 2018. [Cited on page 51.]

[55] Nobuo Sasaki, Muhammad Arif, Yukiharu Uraoka, Jun Gotoh, and Shigeto Sugimoto. Continuous-wave laser lateral crystallization of a-si thin films on polyimide using a heatsink layer embedded in the buffer sio_2. *Journal of Electronic Materials*, 50(6):2974–2980, 2021. [Cited on page 51.]

[56] W. Guo, D. Tang, Y. Liu, J. Wang, and G. Jin. Effect of buffer layer and external stress on magnetic properties of flexible fega films. *Journal of Applied Physics*, 113(17):17B512, 2013. [Cited on page 51.]

[57] S. Hait et al. Spin pumping through different spin–orbit coupling interlayers. *ACS Applied Materials Interfaces*, 14(4):4301–4311, 2022. [Cited on page 51.]

[58] M. Coïsson, F. Celegato, P. Tiberto, and F. Vinai. Magnetic properties of field-annealed feco thin films. *Journal of Magnetism and Magnetic Materials*, 320(20):e739–e742, 2008. Proceedings of the 18th International Symposium on Soft Magnetic Materials. [Cited on page 56.]

[59] Ryan A. O'Dell, Adam B. Phillips, Daniel G. Georgiev, John G. Jones, Gail J. Brown, and Michael J. Heben. Post-deposition annealing effects on ferromagnetic cofeb thin films. *IEEE Transactions on Magnetics*, 54(10):1–7, 2018. [Cited on page 56.]

[60] Lei Lu. *DAMPING MECHANISMS IN MAGNETIC RECORDING MATERIALS MICROWAVE-ASSISTED MAGNETIZATION REVERSAL*. PhD thesis, Colorado State University, 2014. [Cited on page 58.]